



Shock and static pressure demagnetization of pyrrhotite and implications for the Martian crust

Karin L. Louzada^{a,b,*}, Sarah T. Stewart^b, Benjamin P. Weiss^c, Jérôme Gattacceca^d, Natalia S. Bezaeva^e

^a Netherlands Office for Science and Technology, Royal Netherlands Embassy, 4200 Linnean Avenue NW, Washington, D.C. 20008, USA

^b Department of Earth and Planetary Sciences, Harvard University, 20 Oxford Street, Cambridge, MA 02138, USA

^c Department of Earth, Atmospheric and Planetary Sciences, Massachusetts Institute of Technology 54-814, 77 Massachusetts Avenue, Cambridge, MA 02139, USA

^d Department of Geophysics and Planetology, CEREGE (CNRS, Aix-Marseille University), BP 80, 13545 Aix en Provence Cedex 4, France

^e Earth Physics Department, Faculty of Physics, M.V. Lomonosov Moscow State University, Leninskie gory, 119991, Moscow, Russia

ARTICLE INFO

Article history:

Received 11 July 2009

Received in revised form 1 December 2009

Accepted 4 December 2009

Available online 10 January 2010

Editor: T. Spohn

Keywords:

pyrrhotite

Mars

impact cratering

demagnetization

shock

pressure

ABSTRACT

The absence of crustal magnetization around young impact basins suggests impact demagnetization of vast regions of the crust after the cessation of the Martian dynamo. Attempts to understand the impact demagnetization process and to infer the magnetic properties (e.g., the carrier phase) of the Martian crust have been based on the experimental pressure demagnetization of magnetic rocks and minerals. We investigate the magnitude of demagnetization and permanent changes in the intrinsic magnetic properties of single and multidomain natural pyrrhotite under hydrostatic pressures up to 1.8 GPa and shock pressures up to 12 GPa. Both static and dynamic pressures result in an irreversible loss of predominantly low coercivity magnetic remanence. The pressure demagnetization results can be divided into a low-pressure regime and a high-pressure regime. The transition between the two regimes roughly coincides with a ferri- to paramagnetic transition (between 1.2 and 4.5 GPa) and the Hugoniot Elastic Limit (~3.5 GPa) of pyrrhotite. The low-pressure regime is characterized by a decrease in remanence with increasing pressure in both static and shock experiments. The higher pressure regime, probed only by shock experiments, is characterized by a more complicated modification of remanence as a result of permanent changes in the intrinsic magnetic properties of the material. These changes include an increase in saturation remanence and a change in the coercivity distribution towards greater bulk coercivity. Samples that were only submitted to hydrostatic pressure up to 1.8 GPa do not show permanent changes in the magnetic properties. Demagnetization of pyrrhotite as a result of pressure is likely due to a combination of domain reordering (in multidomain grains) and magnetostrictive effects (in single-domain grains). Microfracturing of multidomain grains effectively reduces the domain-size leading to the observed increase in single-domain like behavior. Based on uncertain shock pressure contours around basin-sized craters, impact demagnetization appears to be efficient at only a few GPa. Impact cratering affects the magnetic remanence of crustal rocks on all extraterrestrial bodies. For Mars, the pressure demagnetization results for pyrrhotite indicate that it is a possible carrier of the magnetization in the crust.

© 2010 Elsevier B.V. All rights reserved.

1. Introduction

Impact cratering is a ubiquitous geologic process in the Solar System. The process of impact cratering involves transient stresses that induce phase changes in the bolide and planetary crust and flow fields that lead to the translation and deposition of these materials. The combination of stress and movement also changes the magnetic remanence and magnetic properties of crustal materials.

Impact cratering affects the magnetic remanence of crustal rocks in the following ways. Near the impact point, the impact energy

leads to melting of the bolide and crust, producing a melt sheet lining the basin floor. In the presence of an ambient magnetic field, the melt sheet can acquire a thermoremanent magnetization upon cooling. Outside of the basins, shock pressure decays to levels where heating from the impact is not an important demagnetization mechanism (a few GPa) and nonthermal processes dominate the shock modification of rocks and minerals. In the absence of an ambient magnetic field, the crust may (partially) demagnetize as a result of shock; in the presence of an ambient planetary or strong crustal magnetic field, a shock remanent magnetization may be acquired. Explosive shock experiments on igneous rocks in the Earth's magnetic field indicate that shock remanent magnetization is less efficient than thermoremanent magnetization and that it may be susceptible to viscous decay over geologic time (Gattacceca et al., 2007a). Paleomagnetic evidence of shock remanent magnetization in

* Corresponding author. Netherlands Office for Science and Technology, Royal Netherlands Embassy, 4200 Linnean Avenue NW, Washington, D.C. 20008, USA. Tel.: +1 202 274 2726; fax: +1 202 966 0728.

E-mail address: louzada@post.harvard.edu (K.L. Louzada).

naturally shocked basalts at Lomar crater, India (<50 ka), has been obscured by viscous processes (Louzada et al., 2008). In this study, we will only focus on the process of demagnetization by (transient) pressure.

On Earth, impact demagnetization of the crust is obscured by the remagnetization processes described above. On Mars however, the effects of shock demagnetization may be preserved over geologic time. Large regions of crust devoid of magnetization above and around the youngest impact basins (Hellas, Argyre and Isidis) as observed by the NASA Mars Global Surveyor spacecraft (Acuña et al., 1999; Lillis et al., 2004, 2008b) suggest that impact demagnetization has played an important role in shaping the crustal magnetic field. Based on crater count age estimates (Frey, 2008) of the impact basins, the Martian dynamo ceased ~4 Ga (Lillis et al., 2008a). Estimates of the amplitude of the shock pressures responsible for demagnetization on Mars are based on calculated spatial distributions of shock pressure and spacecraft observations of the distribution of crustal magnetization around impact basins. Preliminary pressure estimates for partial demagnetization around Hellas basin are low, on the order of a few GPa (Hood et al., 2003; Mohit and Arkani-Hamed, 2004; Kletetschka et al., 2004). However, accurate determination of the demagnetizing pressures is sensitive to the poorly constrained formation and collapse processes of impact basins (Louzada and Stewart, 2009). Over Hellas, azimuthally averaged magnetic field profiles suggest that the crust has been completely demagnetized at distances up to 0.8 basin radii (~920 km) and partially demagnetized out to ~1.4 basin radii (~1650 km) (Mohit and Arkani-Hamed, 2004). Considering the uncertainties in Hellas' formation, complete demagnetization is estimated to occur between 1.1 and 3.4 GPa (Louzada and Stewart, 2009).

The potential mineral carriers of the crustal magnetization on Mars are single-domain magnetite, multidomain hematite, and single-domain pyrrhotite (e.g., Dunlop and Arkani-Hamed, 2005). Each potential mineral cannot easily explain the strong intensities of the magnetic anomalies observed over localized portions of the Martian crust (Acuña et al., 1999) without assuming an enriched concentration of magnetic phases with respect to terrestrial crust. Different minerals may dominate or contribute to the magnetic remanence in different locations on Mars. Here, we focus on pyrrhotite.

Pyrrhotite (an iron sulfide) is an important magnetic carrier in magmatic and metamorphic terrains on Earth. It is the main magnetic carrier in the target rock at Bosumtwi Crater in Ghana (Kontny et al., 2007). On Mars, it is likely a primary igneous mineral if the crust and mantle are indeed relatively enriched in iron and sulfur (Longhi et al., 1992). Pyrrhotite is present in all subclasses of Martian meteorites. It is a common phase in the ilmenitic shergottites (McSween Jr and Treiman, 1998 and references therein) and is the principal magnetic carrier in the basaltic shergottites (Collinson, 1986; Rochette et al., 2001, 2005). The latter may be representative of the Martian crust (Longhi et al., 1992). To date, pyrrhotite has not been observed by in situ rover experiments of dust or rocks on Mars or from spacecraft observations (e.g., Bertelsen et al., 2004); however, it may not be preserved at the surface due to oxidation and weathering.

Limited pressure demagnetization experiments have been conducted on pyrrhotite. Under hydrostatic pressures, saturation isothermal remanent magnetization in pyrrhotite has been shown to demagnetize by ~16% in a pyrrhotite-bearing shergottite at 1.24 GPa (Bezueva et al., 2007) and completely in pure pyrrhotite at 3 GPa (e.g., Rochette et al., 2003). However, caution must be used when comparing hydrostatic results to shock-induced demagnetization and then extrapolating to planetary impact cratering. Neither dynamic nor static experiments can reproduce the strain-rate and stress duration conditions that occur during planetary-scale impact cratering. If pressure demagnetization is sensitive to kinetic processes, or directed stress rather than hydrostatic pressure, then the results of the static and dynamic studies may be different. In particular, each

shocked sample undergoes a different pressure loading and unloading path that depends on the achieved shock state.

In this study, we investigate the response of natural pyrrhotite samples to shock pressures up to 12 GPa and hydrostatic pressures up to 1.8 GPa. We report on the magnitude of demagnetization, differences between shock and static experimental results, and permanent changes in the intrinsic magnetic properties of pyrrhotite. We explore the mechanisms responsible for the observed changes and discuss the implications for planetary crustal magnetization.

2. Methods

We performed hydrostatic and shock recovery experiments on three natural pyrrhotite samples: (1) a ~1 cm diameter smooth rounded pure pyrrhotite nodule (No. 98080) from Sudbury, Canada, (2) a euhedral polycrystalline sample (~3×5×1 cm) of pure pyrrhotite with hexagonal habitus and smooth crystal faces (No. 127037) from Chihuahua, Mexico, and (3) a pyrrhotite-bearing metamorphic schist from the Wilson Terrane (Antarctica). In order to determine the changes in remanence and other magnetic properties as a result of pressure, a suite of (magnetic) characterization experiments (Table 1) were conducted on selected samples before and after stress application. Shock experiments on the pure samples (1 and 2) have been briefly discussed in Louzada et al. (2007); the schist (3) has been previously studied in explosive shock experiments up to 30 GPa (Gattacceca et al., 2007b).

2.1. Sample characterization

Pyrrhotite (Fe_{1-x}S , $0 < x < 0.125$) owes its magnetic properties to vacancy ordering in a NiAs crystal structure. When the vacancies are arranged on a superstructure such that alternating layers (001) contain an unequal number of iron atoms, pyrrhotite (Fe_7S_8) exhibits monoclinic symmetry and is ferrimagnetic (Bertaut, 1953) with a strong basal-plane magnetic anisotropy. Other vacancy distributions result in hexagonal symmetry (Fleet, 1968; Morimoto et al., 1975) and usually antiferromagnetic behavior. Natural pyrrhotite contains intergrowths of both magnetic structures of pyrrhotite (Morimoto et al., 1975).

The presence of (monoclinic) pyrrhotite was confirmed in both the polycrystalline sample and the nodule by temperature cycling (Fig. 1) through a magnetic transition at 30 K (Rochette et al., 1990), X-ray diffraction (Table S1) and chemical compositional analyses (Table S2). In the schist, the presence of monoclinic pyrrhotite was confirmed by its Curie temperature (Gattacceca et al., 2007b). Uncompressed (hexagonal) lattice parameters, a and c , are 6.857 ± 0.006 and 22.89 ± 0.06 Å in the nodule and 6.846 ± 0.033 Å and 22.84 ± 0.23 Å in the polycrystalline sample, respectively, consistent with previous studies on pyrrhotite (Dekkers, 1988; Nkoma and Ekosse, 1999). In all specimens, the maximum peak intensity in the X-ray diffraction patterns occurs for the (208) plane, indicative of pyrrhotite. In the polycrystalline sample, a doublet occurs with peaks located at 2.0473 and 2.0615 Å (Fig. S1), indicative of monoclinic pyrrhotite (Yund and Hall, 1969). Based on Fe/S ratios (Table S2), the polycrystalline sample (0.876 ± 0.01) is enriched in monoclinic pyrrhotite ($\text{Fe/S} = 0.875$) with respect to the nodule (0.893 ± 0.01).

Magnetic hysteresis measurements (Table S3) can provide insight into the domain-size of the magnetic fractions. The theoretical ratio of the saturation remanence in zero field, M_{rs} , to the in-field saturation magnetization, M_s , in single-domain (SD, <1.5–2 µm; Menyeh and O'Reilly, 1991; Soffel, 1977) pyrrhotite with triaxial anisotropy confined to the basal plane, is 0.75 (Dunlop and Özdemir, 1997, p.321); although measured values are generally lower than this prediction. The hysteresis data indicate that the nodule is predominantly single domain. However, wasp-waisted hysteresis loops in the nodule indicate a distribution of coercivities (e.g., Dunlop and Özdemir, 1997, p. 316) and a slight increase in remanence at low

Table 1
Overview of sample characterization experiments.

Measurement	Information	Instrument	Tables/figures
X-Ray diffraction patterns ^a	Mineralogy, monoclinic component	Scintag XDS2000 fixed sample position powder diffractometer (Harvard)	Table S1, Fig. S1
Compositional chemistry	Fe/S, mineralogy, monoclinic component	Camica Electron Microprobe (Harvard)	Table S2
Low-T magnetic transitions	Mineralogy, (domain size)	Quantum DC Magnetic Property Measurement System (MIT)	Figs. 1B and 2D in Louzada et al. (2007), Fig. 1
Magnetic hysteresis	Squareness (M_{rs}/M_s), domain size	Micromag Vibrating Sample Magnetometer (CEREGE; IRM, UMN; MIT)	Table S3, Fig. 1A in Louzada et al. (2007)
Anisotropy of magnetic susceptibility	Quantity (degree P') and shape (T) of the susceptibility ellipsoid	Micromag Vibrating Sample Magnetometer and Geofyzika KLY-2 KappaBridge AC Susceptibility Bridge (IRM, UMN)	Table S4, Fig. S3
Uncompressed density	Needed to calculate the principal stress with the impedance match solution	Berman balance (Harvard)	Table 2
Uncompressed sound speeds	Longitudinal and shear wave speeds (c_p and c_s) and Poisson's ratio (ν)	Pulser/receiver method Panametrics Model 500PR with 5 MHz longitudinal (Model V110) and shear wave (Model V156) transducers (Harvard)	Table 2
IRM acquisition ^b	Saturation isothermal remanence	2G Enterprises Superconducting Quantum Interference Device magnetometer with auto sample changers (MIT; Caltech; Yale, CEREGE)*	Fig. 5
AF(z) demagnetization ^c of saturation IRM ^b	Bulk coercivity (MDF) and coercivity distribution	2G Enterprises Superconducting Quantum Interference Device magnetometer with auto sample changers (MIT; Caltech; Yale, CEREGE)*	Figs. 3, 4 and 6
DC demagnetization of saturation IRM	Magnetic interactions between domains	2G Enterprises Superconducting Quantum Interference Device magnetometer with auto sample changers (MIT; Caltech; Yale)*	Fig. S7
Bitter (1931) and magnetic force microscopy	Distribution of ferrimagnetic pyrrhotite, domain size	Optical microscopes, Ferrotec Ferrofluid APG 512 A and carrier fluid M01, Digital Instruments NANOSCOPE III Magnetic Force Microscope (IRM, UMN)	Figs. 7 and S8

^aMeasurements performed on powdered specimens. ^bMeasurements performed on specimens embedded in Al2024 or Al6061 capsule. ^cAn example of the peak alternating field steps is 0.5, 0.7, 1.1, 1.5, 2, 2.5, 3, 4, 6, 8, 10, 13, 17, 20, 25, 30, 36, 42, 48, 55, 63, 71, and 75 mT. *The 2G Enterprises Superconducting Quantum Interference Device magnetometer has a sensitivity of 10^{-12} Am². The samples in this study generally have magnetizations of 10^{-7} – 10^{-4} Am².

temperatures (Fig. 1) indicates a super paramagnetic (SP) fraction. Compared to the nodule, M_{rs}/M_s is lower (0.1479) and B_{cr}/B_c higher (where B_{cr} and B_c are the coercivity of remanence and the bulk coercive force, respectively) in the polycrystalline sample, indicative of multidomain (MD) grains ($>40 \mu\text{m}$; Dekkers, 1988). Finally, the hysteresis parameters indicate that the pyrrhotite grains in the schist are pseudo-single-domain (PSD) (Gattacceca et al., 2007b).

The strong basal-plane magnetic anisotropy of pyrrhotite is evident in the orientation dependence of the hysteresis loops (Fig. S2). Due to

nonlinearity of susceptibility (Hrouda, 2007), low-field anisotropy of magnetic susceptibility in pyrrhotite is field and frequency dependant (Martín-Hernández et al., 2008, and references therein). Anisotropy of magnetic susceptibility (Table S4) was determined from the slopes fit to hysteresis loops between -2.5 and $+2.5$ mT (full range -1 to $+1$ T) in 12 directions. The low-field slopes were then fitted to a second-rank tensor to determine the susceptibility ellipsoid (Jelínek, 1973). The anisotropy degree, P , the ratio of the maximum to minimum principal susceptibilities (κ_1/κ_3) and a measure of the

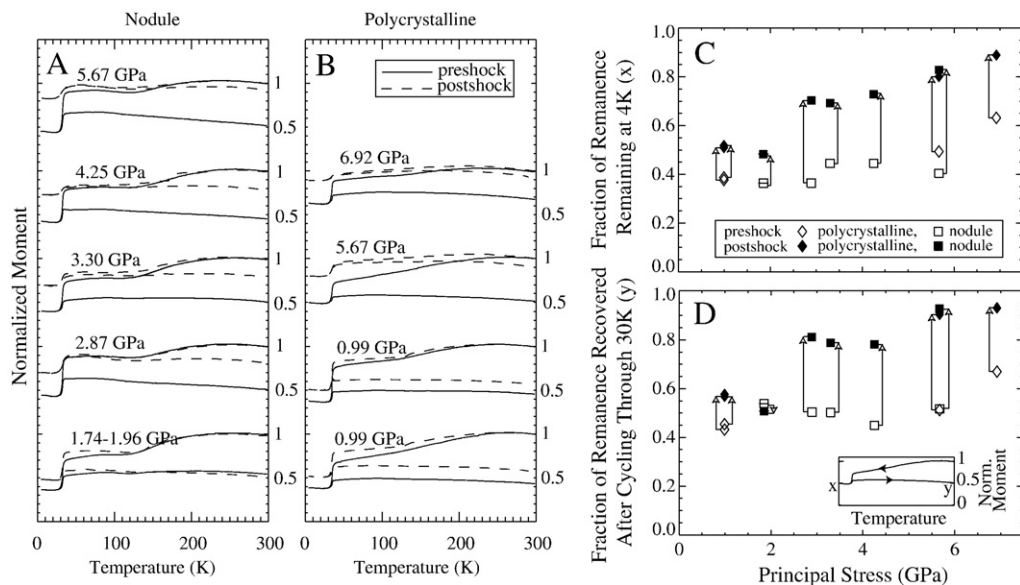


Fig. 1. Low-temperature cycling of preshock (solid) and postshock (dashed) saturation (at 1.5 or 2 T) in the pyrrhotite (A) nodule (No. 98080) and (B) polycrystalline sample (No. 127037) specimens. Changes in the low-temperature memory: (C) fraction of remanence remaining at 4 K ('x' in inset) and (D) fraction of remanence recovered after cycling through the 30 K transition ('y' in inset) versus principal stress in the shock samples. Open symbols denote preshock values, solid symbols — postshock values.

magnitude of anisotropy, is very high in the pure pyrrhotite samples (45.98 in the SD/SP nodule and 56.24 in the MD polycrystalline sample). High anisotropy degrees have also been reported in other large crystal pyrrhotite samples by Martín-Hernández et al. (2008). The shape of the susceptibility ellipsoid is described by the shape factor, $T = 2 [\ln(\kappa_2/\kappa_3)/\ln(\kappa_1/\kappa_3)] - 1$. Since the magnetization is confined to the basal plane, the magnetic fabric in pyrrhotite might be expected to be planar with an

oblate susceptibility ellipsoid ($0 < T < 1$) in a single crystal. This is in fact the case for the unshocked MD sample ($T = 0.697$, Fig. S2) where the easy plane of the susceptibility ellipsoid coincides with the basal plane of the polycrystalline sample inferred from its habit. On the other hand, the susceptibility ellipsoid of the unshocked SD/SP nodule is prolate ($T = -0.776$), indicating a linear magnetic fabric. Oblate, prolate and neutral ($T = 0$) ellipsoids have in fact been observed in other natural pyrrhotites

Table 2

Shock pressure experiments.

Shot	Specimen name ^a	Mass (mg)	Diameter (mm)	Thickness (mm)	Uncompressed density (g/cm ³)	Longitudinal Wave speed (m/s)	Shear wave speed (m/s)	Poisson's ratio ^f
012	98-1A	26.1 (0.05)	3.48 (0.005)	0.668 (0.001)	4.47 (0.046)	4.394 (0.081)	2.852 (0.059)	0.13
019	98-1 K	30.5 (0.03)	2.96 (0.005)	1.02 (0.001)	4.651 (0.01)	4.399 (0.087) ^c	2.873 (0.037) ^c	0.12
020	98-1 L**	28.6 (0.03)	2.91 (0.005)	1.00 (0.001)	4.465 (0.01)	4.399 (0.087) ^c	2.873 (0.037) ^c	0.12
021	98-1H	31.5 (0.03)	2.91 (0.005)	1.07 (0.001)	4.677 (0.01)	4.399 (0.087) ^c	2.873 (0.037) ^c	0.12
022	98-1G	30.6 (0.05)	2.96 (0.005)	1.04 (0.001)	4.655 (0.01)	4.399 (0.087) ^c	2.873 (0.037) ^c	0.12
036	12-A	29.33 (0.002)	3.04–2.97	0.93 (0.001)	4.6077 (0.0105) ^c	4.934 (0.159) ^c	2.631 (0.032) ^c	0.30
036	12-B	37.67 (0.002)	3.09–3.01	1.15 (0.001)	4.6077 (0.0105) ^c	4.934 (0.159) ^c	2.631 (0.032) ^c	0.30
037	12-D	29.74 (0.002)	3.04–3.12	0.90 (0.001)	4.6077 (0.0105) ^c	4.934 (0.159) ^c	2.631 (0.032) ^c	0.30
037	98-1D	27.09 (0.002)	2.54–2.87	1.03 (0.001)	4.612 (0.098) ^h	4.399 (0.087) ^c	2.873 (0.037) ^c	0.12
041	12-E	33.73 (0.002)	3.01–3.12	1.02 (0.001)	4.6077 (0.0105) ^c	4.934 (0.159) ^c	2.631 (0.032) ^c	0.30
041	12-G	36.75 (0.002)	2.99–3.09	1.14 (0.001)	4.6077 (0.0105) ^c	4.934 (0.159) ^c	2.631 (0.032) ^c	0.30
052	12-N*	28.54 (0.002)	2.870 (0.0005)	0.968 (0.0005)	4.6077 (0.0105) ^c	4.887 (0.059) ^d	2.882 (0.021) ^d	0.23
052	12-L	29.26 (0.002)	2.959 (0.0005)	0.950 (0.0005)	4.6077 (0.0105) ^c	4.934 (0.159) ^c	2.631 (0.032) ^c	0.30
053	12-O*	28.57 (0.002)	2.896 (0.0005)	0.996 (0.0005)	4.6077 (0.0105) ^c	4.887 (0.059) ^d	2.882 (0.021) ^d	0.23
053	12-K	29.21 (0.002)	2.985 (0.0005)	0.968 (0.0005)	4.6077 (0.0105) ^c	4.934 (0.159) ^c	2.631 (0.032) ^c	0.30
063	12-C	2147 (1.7)	16 × 19 ^b	1.9228 (0.0062)	4.5724 (0.0173)	5.034 (0.082)	2.706 (0.025)	0.29
064	12-A*	1786 (1.7)	17.5 × 16.5 ^b	2.0984 (0.0072)	4.6074 (0.0081)	4.887 (0.059)	2.882 (0.021)	0.23
067	c5-sf*	221 (1.7)	11.6116 (0.00005)	0.7821 (0.00005)	2.7520 (0.0583)	5.888 (0.021) ^c	3.660 (0.019) ^c	0.18
067	c4-sa	224 (0.5)	11.6872 (0.00005)	0.7652 (0.00005)	2.7583 (0.0592)	5.322 (0.066) ^c	3.174 (0.014) ^c	0.22
068	c5-sg*	197 (0.5)	11.6954 (0.00005)	0.6576 (0.00005)	2.7171 (0.0079)	5.888 (0.021) ^c	3.660 (0.019) ^c	0.18
068	c6-sh	233 (0.5)	11.7580 (0.00005)	0.7859 (0.00005)	2.7786 (0.0050)	5.322 (0.066) ^c	3.174 (0.014) ^c	0.22
Specimen name ^a	Impact velocity (m/s)	Flyer tilt (mrad)	Particle velocity ^g (m/s)	Principal stress ^g (GPa)	Average pressure ^h (GPa)	Notes	Examples in figures	
98-1A	355 (1.16)	2.13 (0.22)	144 (−0.0/+0.4)	3.30 (−0.01/+0.01)	1.42	Initial state demagnetized, remains unmagnetized, broken when removed from capsule	S1A	
98-1 K	300 (1.94)	5.44 (0.45)	121 (−0.6/+1.2)	2.81 (−0.01/+0.01)	1.19	Fractures visible in microscope images	S6A, S8C, S8D	
98-1 L	179–204	~1100	70 (−0.1/+0.4)	1.74–1.96	–	Large flyer tilt, double shock, not included in Fig. 2, RM=0.12	S1A	
98-1H	310 (0.68)	4.21 (0.02)	125 (−0.0/+0.5)	2.89 (−0.01/+0.00)	1.22	–	S1A, S6B	
98-1G	461 (1.52)	4.11 (0.63)	190 (−0.1/+0.7)	4.25 (−0.02/+0.01)	1.80	–	S1A, S4	
12-A	749 (9.71)	12.8 (2.90)	317 (−3.8/+4.3)	6.92 (−0.09/+0.08)	4.28	Broken when removed from capsule	4C, S1B	
12-B	749 (9.71)	12.8 (2.90)	317 (−3.8/+4.3)	6.92 (−0.09/+0.08)	4.28	Broken when removed from capsule	–	
12-D	615 (18.3)	12.4 (3.64)	258 (−7.4/+7.9)	5.67 (−0.17/+0.17)	3.51	–	S1B, S6D	
98-1D	615 (18.3)	12.4 (3.64)	258 (−7.4/+7.9)	5.67 (−0.17/+0.17)	2.40	–	3A, 4A and 4B, S1A, S6C, S7A, S7B, S8Q, S8R	
12-E	92.6 (0.28)	–	35 (−0.2/+0.2)	0.99 (−0.00/+0.00)	0.61	Erratic Zijderveld plot, broken when removed from capsule	S1B	
12-G	92.6 (0.28)	–	35 (−0.2/+0.2)	0.99 (−0.00/+0.00)	0.61	–	S1B	
12-N*	1054 (6.53)	6.15 (15.0)	457 (−2.3/+2.8)	9.83 (−0.07/+0.06)	5.23	–	7I and 7 J, S7C	
12-L	1054 (6.53)	6.15 (15.0)	457 (−2.3/+2.8)	9.83 (−0.07/+0.06)	6.08	–	3B, 7 K, 7 L, S6E	
12-O*	1284 (22.6)	24.6 (0.54)	566 (−10.0/+10.4)	12.0 (−0.23/+0.22)	6.38	–	7E and 7F	
12-K	1284 (22.6)	24.6 (0.54)	566 (−10.0/+10.4)	12.0 (−0.23/+0.22)	7.42	–	7G and 7H	
12-C	1156 (53.6)	0.36 (0.03)	505 (−24.3/+25.0)	10.8 (−0.53/+0.53)	6.54	HEL measurement	S5	
12-A*	1171 (7.25)	3.77 (6.52)	511 (−2.4/+3.0)	10.9 (−0.08/+0.07)	5.80	HEL measurement	S5	
c5-sf*	1192 (21.3)	3.59 (1.61)	587 (−10.1/+10.7)	10.1 (−0.20/+0.19) ⁱ	4.84	–	–	
c4-sa	1192 (21.3)	3.59 (1.61)	587 (−10.1/+10.7)	10.1 (−0.20/+0.19) ⁱ	5.26	–	3C and 5A	
c5-sg*	466 (0.57)	4.38 (1.27)	229 (−1.1/+1.6)	3.76 (−0.02/+0.01) ⁱ	1.80	–	–	
c6-sh	466 (0.57)	4.38 (1.27)	229 (−1.1/+1.6)	3.76 (−0.02/+0.01) ⁱ	1.96	–	–	

*Shock direction parallel to foliation (in schist) or easy plane of magnetization (in pure minerals). ** Shocked twice. ^aAbbreviated sample names: '98' = D/SP nodule (No. 98080), '12' = MD polycrystal (No. 127037), 'cx-xx' = PSD pyrrhotite-bearing schist. ^bApproximate dimensions. ^cOn bulk sample. ^dFrom 12-A*. ^eAverage of five specimens. ^fPoisson's ratio, $\nu = 1/2(c_p^2 - 2c_s^2)/(c_p^2 + c_s^2)$, where c_p and c_s are the longitudinal and shear wave speeds respectively. ^gPlanar impact approximation between aluminum flyer and capsule and between shocked capsule and sample (Melosh, 1989, p. 54–57). ^hThe average pressure, $P = (\sigma_1 + 2\sigma_2)/3 = \frac{1}{3}[(1 + \nu)/(1 - \nu)]\sigma_1$, where σ_1 is the principal stress, the perpendicular stresses are $\sigma_2 = \sigma_3$, and ν is the Poisson's ratio. ⁱPrincipal stress assumed to be the same as in aluminum.

(Martín-Hernández et al., 2008). Anisotropy of magnetic susceptibility of the PSD pyrrhotite-bearing schist is much smaller ($P = 1.741$), within the range of previous measurements on schists (e.g., Hrouda, 2007) and is oblate ($T = 0.697$) as would be expected if the pyrrhotite grains grew with their basal-plane (001) roughly parallel to the foliation in the rock.

2.2. Planar shock recovery experiments

Shock recovery experiments were conducted in the ambient magnetic field in the target tank (12.7 μT directed up-range, or antiparallel to the propagation direction of the shock wave) on disc-shaped (~3 mm diameter, ~1 mm tall) polycrystalline and nodule specimens, and (~12 mm diameter, ~1 mm tall) schist specimens at pressures up to 12 GPa (Table 2). A subset of the data was discussed in Louzada et al. (2007). Prior to shock demagnetization, isothermal remanence was acquired in magnetic fields of 390 to 1100 mT, resulting in (near-) saturation of the specimens. Six specimens of the SD/SP nodule were cored from two subparallel slices cut at an angle of ~14–30° between the normal of the plane of the disc and the easy-axis of magnetization. Nine specimens of the MD polycrystalline sample were cut from two slices with the plane of the disc being either (within 10°) perpendicular or parallel to the easy plane of magnetization. The easy plane of magnetization makes an angle of 44–48° with the plane of the disc in four PSD schist samples.

Shock was induced by aluminum (Al6061) flyer plates (34 to 38 mm diameter and 3 mm thick) atop ~75-mm long polycarbonate sabots that were accelerated to 180–1250 m/s using compressed helium in the 40-mm, single-stage gas gun in the Harvard Shock Compression Laboratory (Stewart, 2004). The magnetic specimens were embedded in aluminum capsules (6–20 mm in diameter and 9–19 mm tall). The capsules have a minimal affect on the magnetic measurements; for the least magnetic samples (schists) only 5.1–9.7% of saturation isothermal remanence is attributed to the aluminum. The cylindrical symmetry of the target assembly and lateral and rear momentum traps ensure that the wave profiles in the specimens are planar with minimal interference from reflections (Figs. S3 and S4).

Peak shock pressure (principal stress, σ_1) in the specimen is determined using the impedance match solution (Melosh, 1989, p. 54–57) and the material shock parameters in Table S5. In elastic solids, the longitudinal (principal) stress wave is accompanied by two orthogonal, transverse stress waves of lower amplitude (σ_2 and σ_3 , $\sigma_2 = \sigma_3$). The average pressure, P , in the specimen is: $P = \frac{1}{3}(\sigma_1 + 2\sigma_2) = \frac{1}{3}\sigma_1(1 + \nu)/(1 - \nu)$. The dimensionless Poisson's ratio, ν , can

be determined from the longitudinal sound speed (c_p) and shear wave speed (c_s) (Table 2). As average pressure increases, the difference between the longitudinal and transverse stresses increases until the Hugoniot Elastic Limit is reached, and the shear stress [$\tau = (\sigma_1 - \sigma_2)/2$] no longer increases. At this point, elastic and plastic deformation take place simultaneously. For strong pressure waves, the difference between the longitudinal and transverse stresses is small compared to the mean stress so that $P \sim \sigma_1$. We performed laser velocity interferometer experiments on the MD polycrystalline sample and determined a Hugoniot Elastic Limit of ~3.5 GPa for pyrrhotite (Fig. S5), comparable to that of basalt (e.g., 2 GPa; Sekine et al., 2008).

2.3. Hydrostatic pressure demagnetization experiments

Hydrostatic pressure demagnetization of saturation isothermal remanence (acquired in a >3 T field) in the pure pyrrhotite samples was conducted using nonmagnetic ("Russian" $\text{Ni}_{57}\text{Cr}_{40}\text{Al}_3$ /Ti-alloy) composite high-pressure cells of piston-cylinder type (Sadykov et al., 2008) up to 1.24 or 1.8 GPa. Pressure experiments on the schist are reported in Bezaeva et al. (in press). The advantage of experiments using these cells is that the small size (outer diameter ~30 mm) allows it to be placed inside a 2G Enterprises SQUID magnetometer so that remanence measurements can be made while under pressure as well as upon decompression. Hydrostatic compression up to 1.24 or 1.8 GPa (depending on the operating pressure limit of the cell used) was applied in a near zero magnetic field (<5 μT) to avoid acquisition of a piezo-remnant magnetization. As a transmitting-pressure medium, we used the inert polyethylsiloxane (PES-1) liquid (Kirichenko et al., 2005).

3. Results

3.1. Pressure demagnetization

Both dynamic (Table 2) and static (Table 3) pressures result in a loss of magnetic remanence in pyrrhotite (Fig. 2A and B). Hydrostatic pressure demagnetization trends of absolute magnetic intensity overlap significantly below 1.24 GPa for samples with different domain sizes (open grey symbols; measurements upon decompression are indicated by solid grey symbols). Complete demagnetization is achieved at ~2.8 GPa (Rochette et al., 2003). The demagnetization occurs upon compression and is mostly irreversible; only 3–6% of the initial remanent magnetization is recovered upon decompression from 1.24 GPa (Table 3; Bezaeva et al., 2007; in press).

Table 3
Static pressure experiment demagnetization results.

Sample	MD polycrystal		SD NWA1068 Martian meteorite ^a		PSD Schist ^b	PSD NWA753 Rumuruti chondrite ^b		MD Synthetic Powder ^b		SD/SP nodule		SD pure Ducktown ^c	
Pressure (GPa)	M ($\times 10^{-1}$)	RM	M ($\times 10^{-2}$)	RM	RM	M ($\times 10^{-2}$)	RM	RM	RM	Pressure (GPa)	RM*	Pressure (GPa)	RM*
0	8.33	1.00	10.6	1.00	1.00	3.68	1.00	1.00	1.00	0	1.00	0	1.00
0.15	8.19	0.982	10.4	0.989	1.00	3.61	0.982	0.946	0.903	0.18	0.94	1	0.426
0.31	8.19	0.983	10.2	0.970	0.95	3.60	0.978	0.882	0.839	0.36	0.94	2	0.224
0.46	7.98	0.957	10.0	0.949	0.93	3.55	0.964	0.839	0.796	0.72	0.89	2.5	0.156
0.62	7.78	0.934	9.72	0.921	0.90	3.48	0.944	0.807	0.775	0.90	0.87	2.75	0.029
0.77	7.54	0.905	9.47	0.898	0.87	3.45	0.938	0.796	0.753	1.08	0.82	3	0
0.93	7.29	0.875	9.38	0.889	0.86	3.44	0.934	0.775	0.742	1.26	0.78		
1.08	6.93	0.831	9.04	0.856	0.82	3.36	0.912	0.753	0.721	1.44	0.75		
1.24	6.68	0.802	8.80	0.834	0.78	3.33	0.904	0.732	0.710	1.8	0.7		
0	6.93	0.832	9.14	0.866	0.84	3.38	0.917						
1.24	6.39	0.767											
0	6.72	0.807											
mass (mg)	24.5		240.2		–	211.9		33.5	32.8	–		34–64	

M = Absolute magnetization (Am^2/kg). RM = Fraction of initial magnetization remaining. ^a(Bezaeva et al., 2007). ^b(Bezaeva et al., in press). ^c(Rochette et al., 2003). * Remaining magnetization upon decompression. SD = Single-domain. PSD = Pseudo-single-domain. MD = Multidomain.

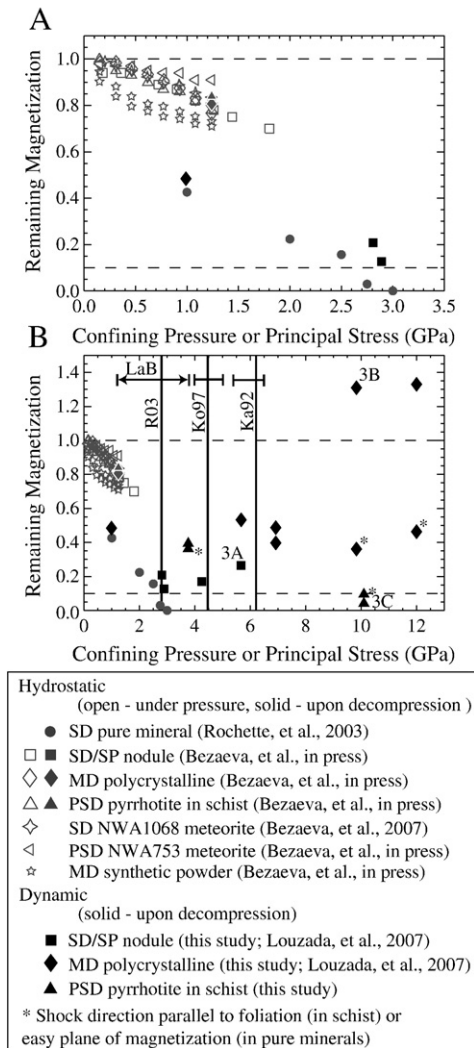


Fig. 2. Demagnetization results of hydrostatic and dynamic experiments on pyrrhotite. Panel (A) is a detail of (B). Shocked samples are considered to be completely demagnetized if the remaining magnetization level is below 10%, due to the pressure distribution in the samples (Fig. S4). Zijderveld alternating field demagnetization plots of selected samples labeled '3A', '3B' and '3C' are shown in panels A, B and C of Fig. 3, respectively. Vertical lines indicate (magnetic) phase transitions observed in hydrostatic experiments (Ka92 = Kamimura et al., 1992; Ko97 = Kobayashi et al., 1997; LaB = LaBounty et al., submitted; R03 = Rochette et al., 2003).

Demagnetization levels in shocked samples were determined using the total vector lengths of the alternating field demagnetization trends of the pre- and postshock remanences (Fig. 3A). (Remaining magnetization fractions determined using absolute intensities yield results that differ by 2–4.3% in the SD/SP nodule, 0.4–7.8% in the MD polycrystalline sample and 0–1% in the PSD schist.) Below ~3 GPa, hereafter the low-pressure regime, the pure mineral results are remarkably consistent with the static demagnetization data (Fig. 2A), despite there being some scatter in the data between static and shock experiments at 1 GPa. Above ~3 GPa, the high-pressure regime, shock does not result in complete demagnetization of pyrrhotite (Fig. 3B). In fact, the remaining remanence in the pure mineral phases increases with increasing pressure in the high-pressure regime. This result cannot be attributed to the production of quenched metastable ferrimagnetic hexagonal pyrrhotite (Bennet and Graham, 1981) as heating was insufficient (<210–230 °C) to generate this phase upon cooling. Also, it cannot be a result of the of shock remanent magnetization acquired in strong impact-generated fields because

the impact velocities were much lower than those shown to produce plasmas (multiple km/s; Crawford and Schultz, 1988). Further, one specimen that had been demagnetized prior to being shocked did not acquire a remanence at 3.30 GPa. Finally, postshock remaining remanences do not possess a second component of magnetization parallel to the direction of the ambient laboratory field (Fig. 3).

The net increase in remanence in two outlying shocked specimens (in the high-pressure regime) of the MD polycrystalline sample (Fig. 2B) may be related to the simultaneous effect of increased single-domain like behavior (Section 3.2) and orientation differences in efficiency of irreversible damage to magnetic domains (Section 4.3). When the PSD pyrrhotite-bearing schist with a much lower anisotropy of magnetic susceptibility (Table S4) is shocked in two perpendicular directions, the results do not show orientation dependence.

Alternating field demagnetization curves (Fig. 4A) provide insight into changes in the coercivity of pyrrhotite, and the slopes of the demagnetization curves (the coercivity spectra, Fig. 4B) provide information about the changes in the coercivity distribution in the sample. Demagnetization curves of postshock remaining magnetization (solid line) are flat at low peak field levels, indicating no magnetic remanence is removed at these levels during alternating field demagnetization, as it has been preferentially removed as a result of pressure. In comparison, the preshock saturation remanence curve (dashed line) has a negative slope. The coercivity fraction demagnetized by 5.67 GPa shock in the SD/SP nodule is located between 0 and 15 mT (horizontal arrow in Fig. 4B) consistent with previous pressure studies of magnetic minerals (e.g., Cisowski and Fuller, 1978; Jackson et al., 1993).

The transition between the low-pressure regime and the high-pressure regime approximately coincides with the Hugoniot Elastic Limit of pyrrhotite at ~3.5 GPa. Several static pressure studies observed a reversible magnetic transition to paramagnetism near this pressure (Fig. 2B). However, differences in the transition pressures are likely due to differences in pressure calibration methods, equilibration time scales, non-hydrostatic contributions to stress, and/or sample differences. The transition was observed at 4.5 ± 0.5 GPa (Kobayashi et al., 1997) and between 1.2 and 3.8 GPa (Dierdre La Bounty and Sang-heon Shim, personal communication) in Mössbauer spectroscopy, and in neutron diffraction experiments between 2.6 and 3.1 GPa (Rochette et al., 2003). X-ray diffraction measurements under pressure indicate a change in lattice compressibility, but not a discontinuous volume change, at 4.5 ± 0.5 GPa (Kobayashi et al., 1997) and at 6.2 GPa (Kamimura et al., 1992). Because lattice parameters of the postshock (recovered) SD/SP nodule (5.67 GPa) and MD polycrystalline sample (6.92 GPa) are within error the same as their uncompressed equivalents (Table S1), we cannot rule out a reversible transition did not occur. Earlier Mössbauer spectroscopy experiments placed the transition between 0.5 and >1.6 GPa (Vaughan and Tossell, 1973). The onset of a first-order phase change to a high-pressure phase was detected in shock experiments between 2.7 and 3.8 GPa (Ahrens, 1979, also with uncertain pressures, T. Ahrens, personal communication).

The slope of demagnetization with pressure above 1.24 GPa is uncertain. Static pressure demagnetization of one pyrrhotite sample (No. 98080, open grey squares in Fig. 2) with a new nonmagnetic pressure cell capable of making magnetic measurements up to 1.8 GPa suggests that the demagnetization slope is constant below 2 GPa. Both the slope of the demagnetization trend at greater pressures and whether the static data approach the shock data is unknown at present.

3.2. Permanent changes in the magnetic properties of shocked pyrrhotite

Shock compression induces permanent changes in the intrinsic magnetic properties of pyrrhotite. After shock, the material can acquire a greater remanence when strong fields are applied, as

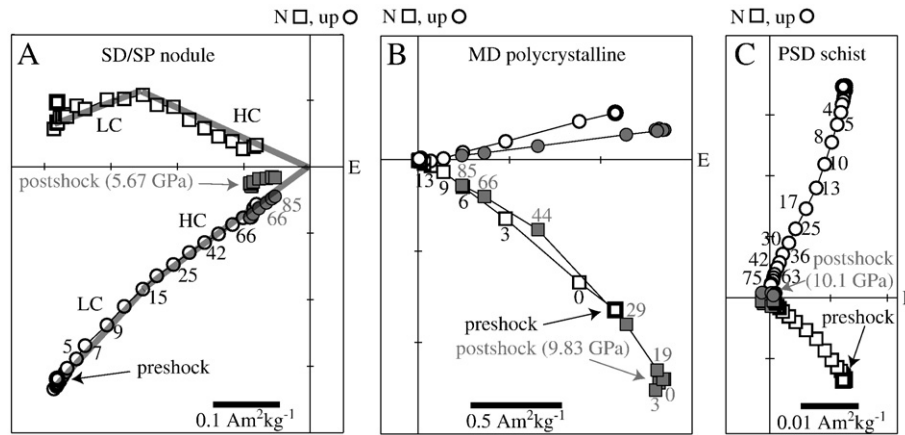


Fig. 3. Example orthogonal (Zijderveld) projection plots of alternating field demagnetization of preshock (saturation isothermal) remanence (black) and postshock remaining remanence (grey) in specimens of the (A) SD/SP nodule (98080-1D), (B) MD polycrystalline sample (127037-L), and (C) PSD schist (c4-sa). Squares indicate horizontal projections on the E-N plane; circles indicate projections on the E-vertical plane. The preshock remanence in the SD/SP nodule consists of two components, a low coercivity component (LC) removed by peak alternating fields up to ~15 mT, and a high coercivity component (HC) removed at higher fields. Pre- and postshock remanence intensities were determined by summing the total vector lengths (e.g., $|LC| + |HC|$) of the demagnetization plots. A high coercivity component (1–20% of the saturation remanence) remains in the pyrrhotite-bearing samples upon maximum AF cleaning (75–95 mT). Numbers indicate peak alternating fields in mT.

illustrated by the isothermal remanent magnetization acquisition curve in Fig. 5A. Generally, samples shocked above a few GPa in the high-pressure regime demonstrate an increase in saturation remanence with pressure, although, there is significant scatter in the magnitude of the increase (Fig. 5B). Increase in saturation remanence is consistent with an increase in M_{rs}/M_s observed in the MD polycrystalline sample (Table S3; Louzada et al., 2007) and the PSD schist (Fig. 6 in Gattacceca et al., 2007b). The average M_{rs}/M_s ratios in the shocked SD/SP nodule are within 1 σ error of the unshocked nodule, with the exception of one specimen shocked at 2.81 GPa.

Changes in coercivity of pyrrhotite are indicated in Figs. 4 and 6. Postshock resaturation remanence spectra are broader than preshock spectra (compare the grey and dash-dotted lines in Fig. 4B and C), with their peaks displaced towards higher peak alternating field values. The saturation remanent magnetization after shock is carried by fractions with a wider range of coercivities, and the bulk of the magnetization is removed at greater fields than in the unshocked case. All shocked specimens, except for one at low pressure (0.99 GPa), show an increase in the median destructive field (the magnetic field required to remove half of the magnetization) and the peak field of the coercivity spectra of saturation remanence after shock (compare open symbols to closed symbols in Fig. 6A and B). With increasing shock pressure, the magnitude of both quantities increases.

In addition to the changes shown here, previous work has also shown an increase in the low-temperature memory of shocked pyrrhotite as it is cycled through the low-temperature transition at ~30 K (Fig. 1; Louzada et al., 2007). Both the fraction of remanence remaining at 4 K and the fraction of remanence recovered upon cycling through 30 K increase as a result of shock (Fig. 1C and D), particularly in the high-pressure regime, indicative of an effective decrease in grain size (Dekkers et al., 1989). The changes observed are consistent with stress (or shock) hardening of the material. Increasing coercivity, saturation remanence, M_{rs}/M_s and low temperature memory of pyrrhotite have been shown to correlate with decreasing grain and domain-size (Dekkers, 1988, 1989; Dekkers et al., 1989). Increasing single-domain like behavior of shocked and stressed materials has been observed in titanomagnetite bearing samples (e.g., Cisowski and Fuller, 1978; Jackson et al., 1993; Gilder et al., 2004) and may be a sensitive indicator of shock in originally multidomain materials. Note that (within error) the change in M_{rs}/M_s in the single-domain nodules is negligible (Table S3; Louzada et al., 2007).

4. Discussion

4.1. Stress effects on pyrrhotite

Here we discuss the similarities of the results of our work with previous studies on the effects of stress on magnetization. Hydrostatic experiments capable of measuring remanent magnetization while under pressure show that demagnetization of initial (before compression) magnetization occurs predominantly upon the application of stress, rather than upon decompression, and is mostly irreversible (Bezaeva et al., 2007; see also quasi-hydrostatic results on MD magnetite in Gilder et al., 2006). Recovery of remanence upon decompression is only a few percent in the pyrrhotite samples investigated here. Although repeated stress cycling will reduce the magnetization further, the bulk of the remanence loss occurs upon the first application of stress, e.g., a second application of 1.24 GPa decreases the remaining remanence from 83% to 80% in the MD polycrystalline sample (open diamonds in Fig. 2A).

In multidomain samples, magnetic domain reordering upon static compression, which is irreversible upon decompression, may reduce magnetization (e.g., Nagata and Carleton, 1969; Borradaile and Jackson, 1993). The fact that the rockmagnetic properties of hydrostatically stressed samples in the low-pressure regime do not change (e.g., saturation remanence and coercivity, Figs. 5 and 6; Bezaeva et al., 2007, *in press*) indicates that the domain reordering is reversible upon resaturation (the domain walls move to their original positions). This observation is consistent with the fact that no permanent deformation or damage was observed upon visual inspection of statically stressed pyrrhotite up to 3 GPa (Rochette et al., 2003).

In single-domain grains, pressure demagnetization cannot be attributed to domain wall movements. Rather, changes in magnetostriction and magnetocrystalline anisotropy have been invoked as a pressure demagnetization mechanism (e.g., Nagata, 1966; Kinoshita, 1968; Gilder et al., 2004). Magnetocrystalline anisotropy is the result of crystallographic symmetry of ferromagnetic minerals and magnetostriction is the spontaneous change in shape of a crystal lattice when magnetized as a consequence of the strain dependence of magnetocrystalline anisotropy (e.g., Dunlop and Özdemir, 1997, p. 42). Materials with a positive magnetostriction expand in the direction of a magnetic field and contract in the transverse directions. If the lattice is constrained however, e.g., due to an external stress, then magnetostriction will not be accommodated and magnetostrictive

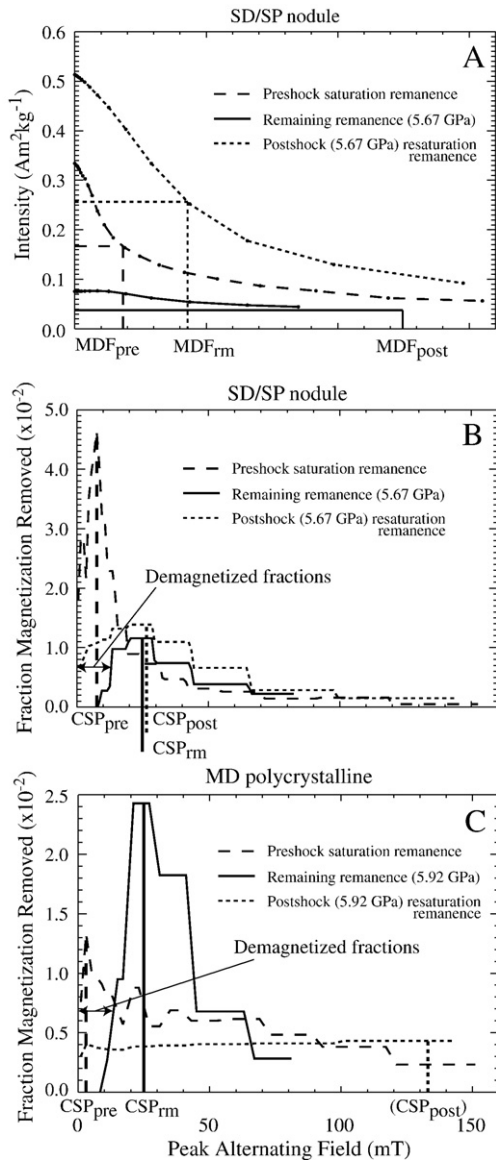


Fig. 4. (A) Example alternating field demagnetization curves of the z-component of preshock remanence (dashed), postshock remaining magnetization (black) and postshock resaturation remanence (dotted) for a SD/SP nodule specimen (98080-1D). MDF_{pre} , MDF_{rm} and MDF_{post} (extrapolated) are the median destructive fields of the magnetic remanences. (B and C) Coercivity spectra of magnetization removed in 1 mT bins of the magnetic remanences derived from the alternating field demagnetization curves. CSP_{pre} , CSP_{rm} , CSP_{post} are the fields at which the peaks of the coercivity spectra are located. CSP_{post} in C is ill defined.

strain energy arises (Nagata and Kinoshita, 1967). The field required to overcome this magnetostrictive energy increases with external stress. In the absence of a field, the spontaneous magnetization in the crystal will rotate away from the stress axis. If there were no internal stresses in crystals, then we would expect the stress effects on remanence to be reversible upon decompression and equal with each application of stress. However, our observations of irreversibility and decreasing efficiency of demagnetization with the number of stress cycles imply that threshold energies for domain restructuring are locally overcome (e.g., Kinoshita, 1968).

4.2. Grain damage

The two specimens that were subjected to hydrostatic compression up to 1.24 or 1.8 GPa (in the low-pressure regime) do not show any permanent changes in their magnetic properties, probably because the

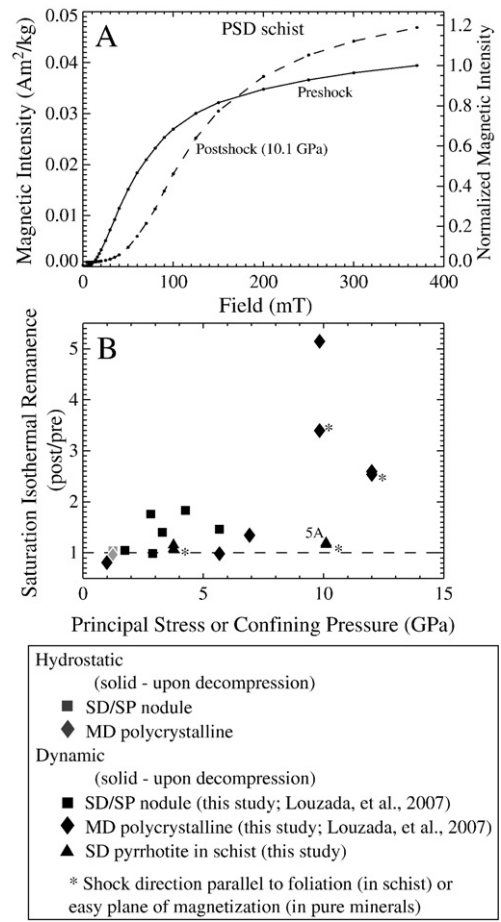


Fig. 5. (A) An example of saturation isothermal remanent magnetization acquisition curves up to 380 mT in unshocked (solid) and postshock (9.96 GPa, dashed) PSD schist (c4-sa). The Al2024 capsule makes up 9.7% of the magnetic moment. (B) Change in saturation isothermal remanence of specimens subjected to static and shock compression. Specimen shown in panel A is labeled '5A' in panel B.

pressures were too low to cause irreversible deformation or damage to the pyrrhotite. Pyrrhotite recovered upon decompression from 3 GPa in quasi-hydrostatic experiments did not show any signs of significant shape change or loss of coherence upon visual inspection either (Rochette et al., 2003). In contrast, pervasive fracturing was observed in microscope images of the nodule, polycrystalline, and schist specimens shocked to pressures over 2.81 GPa (Fig. S6) and in the high-pressure regime. Fracturing can be more intense around the outer perimeter of the disc-shaped specimen, radial, or make 60° angles.

Microfracturing has been invoked in experimentally shocked (explosive) magnetite-bearing rocks as a cause of hysteresis modification (Gattacceca et al., 2007b). Fracturing and/or dislocation/defect generation impeding motion of domain walls has also been invoked in hydrostatic stress experiments up to 6 GPa (Gilder et al., 2004; Gilder and Le Goff, 2008). If dilatational fractures subdivide large grains into smaller multidomain or single-domain grains, then fracturing may lead to the observed magnetic hardening. An evaluation of the types of magnetic interactions between the domains in the pyrrhotite before and after shock (Fig. S7) indicates that the changes in interactions in the MD pyrrhotite are consistent with a decrease in grain size (a decrease in the net demagnetizing effect). Changes in domain interactions in the nodule are much smaller.

4.3. Magnetic domain imaging

In Bitter (1931) imaging, magnetic colloid is attracted to domain and grain boundaries making them appear dark in the image, whereas

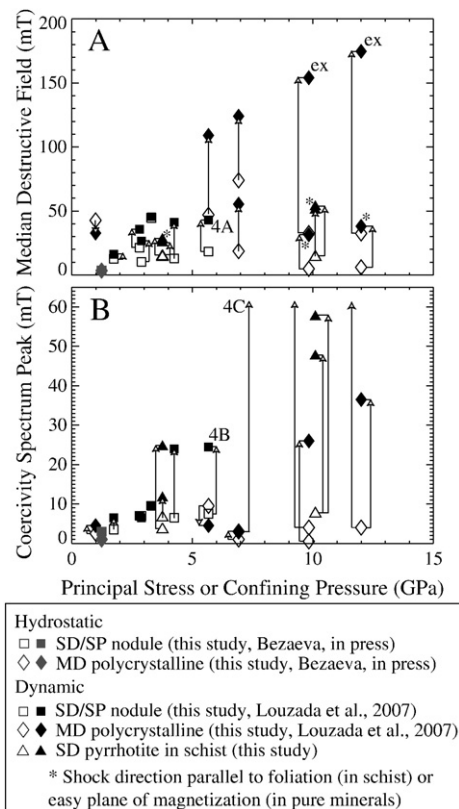


Fig. 6. Pre- (open symbols, MDF_{pre}) and postcompression (solid symbols, MDF_{post}) median destructive fields (MDF) of saturation remanence of static compressed (grey symbols) and shocked (black symbols) pyrrhotite samples. The postshock MDF of 127037-L and -K were extrapolated (labeled 'ex'). The grey open and solid symbols are overlapping, indicating no change in MDF. Example AF demagnetization plots and coercivity spectra are shown in Fig. 4A–C, labeled '4A', '4B', and '4C'.

homogeneously magnetized or nonmagnetic regions appear bright. The magnetic monoclinic pyrrhotite in the polycrystalline sample is organized into long, thin stripes (30–55 μm wide and up to >1 mm long) mutually intersecting at $\sim 60^\circ$, intergrown with antiferromagnetic (nonmagnetic) hexagonal pyrrhotite (Fig. 7A) (Soffel, 1981; Pósfai et al., 2000). Assuming that these magnetic stripes continue in the c -plane (perpendicular to the page), the stripes are interpreted as lamellae (sub-) parallel to (001) (the basal plane, Kontny et al., 2000, and references therein). Higher resolution magnetic force microscopy images of the magnetic lamellae (Fig. 7B) reveal a set of simply arranged parallel dark and bright lines, with a spatial scale of $\sim 1 \mu\text{m}$ by 12 to 33 μm (but possibly longer), corresponding to regions where magnetic flux is going into or coming out of the plane, respectively, and are interpreted as magnetic domains (e.g., Bennet et al., 1972) separated by walls in which the magnetization rotates 180° . Other observations of average domain width in pyrrhotite are variable: ~ 4 – $8 \mu\text{m}$ (Halgedahl and Ye, 2000) and 100–200 nm (Pósfai et al., 2000). Pósfai et al. (2000) observed large scale lamellae widths of $\sim 30 \mu\text{m}$, similar to the lamellae reported above. Bitter and magnetic force microscopy images of the surface parallel to (001) of the unshocked MD polycrystalline sample show broad regions of grey, indicating magnetization is mostly confined to the plane (Fig. 7C and D), consistent with pyrrhotite having a strong magnetocrystalline anisotropy. The unshocked SD/SP nodule has smaller, often isolated, acicular lamellae, which also mutually intersect at $\sim 60^\circ$ angles (Fig. S8), consistent with its SD like magnetic properties.

Bitter images of specimens shocked in the high-pressure regime (Fig. 7E and I) reveal pervasive fracturing. Magnetic force imaging indicates that the magnetic domains are still sub-parallel to (001), but that the boundaries between the domains undulate (Fig. 7F and J).

Sinuous lines (white arrows in Fig. 7F) cross-cut the lamellae, and although the widths of the lamellae have not changed (<1 to $2 \mu\text{m}$), the lengths of the domains appear to be shorter. The perpendicular view (001) shows broad swaths of chaotic bright and dark regions (Fig. 7H and L). Due to the isolated distribution of smaller domains in the preshock nodule, it is hard to draw conclusions from the postshock recovered nodule images (Fig. S8).

Due to the strong magnetocrystalline anisotropy, the domain patterns of pyrrhotite are insensitive to thinning or stresses induced by polishing (Halgedahl and Ye, 2000). Progressively higher peak AF demagnetization normally results in more planar 180° domain walls and a simpler domain distribution in pyrrhotite (Halgedahl and Fuller, 1981). The fact that the domains in the AF demagnetized (~ 85 mT) shocked pyrrhotite are undulating, suggests that the domain walls are pinned and cannot move to a more energetically favorable parallel arrangement under alternating fields. Soffel (1981) found that curved domain walls occur only in regions of high inclusion or dislocation density. Planar defect structures, kink-bands and banded twin lamellae in pyrrhotite in a polymict impact breccia from Bosumtwi crater (Kontny et al., 2007) were also attributed to brittle and/or brittle–ductile deformation features and nanoscale fracturing resulting from differential stresses associated with the shock wave. Such shock-induced substructures have been invoked to explain the magnetic hardness of pyrrhotite in the Martian shergottite meteorites as well (Rochette et al., 2001).

4.4. Generalization of the results

Overall, the low-pressure regime demagnetization effects seen in this study are similar to those observed for other previously studied magnetic phases. Low coercivity magnetization is preferentially demagnetized in all minerals (Cisowski and Fuller, 1978; Louzada et al., 2007; Bezaeva et al., 2007, in press; Gattacceca et al., 2007b) upon compression (Nagata and Kinoshita, 1964; Nagata, 1966; Bezaeva et al., 2007). Repeated low-pressure shock experiments of igneous rocks also indicate that the first application of stress results in the greatest loss of initial remanence (Nagata, 1971; Pohl et al., 1975). Magnetic hardening has been proposed as a potential magnetic indicator of low shock (a few GPa) in magnetic minerals (Jackson et al., 1993; Gilder et al., 2004; Kontny et al., 2007) and in multidomain fractions in naturally shocked basalts (Cisowski and Fuller, 1978; Louzada et al., 2008). The use of shocked magnetic minerals as indicators of paleofield intensity is complicated by the fact that both magnetic remanence and magnetic properties are affected by shock.

A compilation of demagnetization experiment results suggests that pressure demagnetization levels of different minerals (titanomagnetite, titanohematite and pyrrhotite) are not unique at low pressures (Louzada et al., submitted) and therefore not predictable a priori. However, within each mineral group, the demagnetization at 1.24 GPa is a function of coercivity and roughly proportional to $\ln(B_{cr})$ (Bezaeva et al., in press). Different demagnetization mechanisms (e.g., grain brecciation and domain movement and nucleation) may be active in different minerals and, within a single mineralogy, demagnetization may be composition, domain state and/or phase dependant.

4.5. Implications for the Martian crust

The crustal magnetic field remains an enigmatic feature of Mars. At present, Mars no longer possesses a global magnetic field. However, the presence of crustal magnetic fields observed by the NASA Mars Global Surveyor spacecraft (Acuña et al., 1999; Lillis et al., 2004, 2008b) and the identification of magnetization in Martian meteorites (Weiss et al., 2002, 2008; Antretter and Fuller, 2002; Gattacceca and Rochette, 2004) suggests that it did in the past. The majority of the crustal magnetic anomalies are located in the heavily cratered southern hemisphere and the intensities of the magnetic anomalies

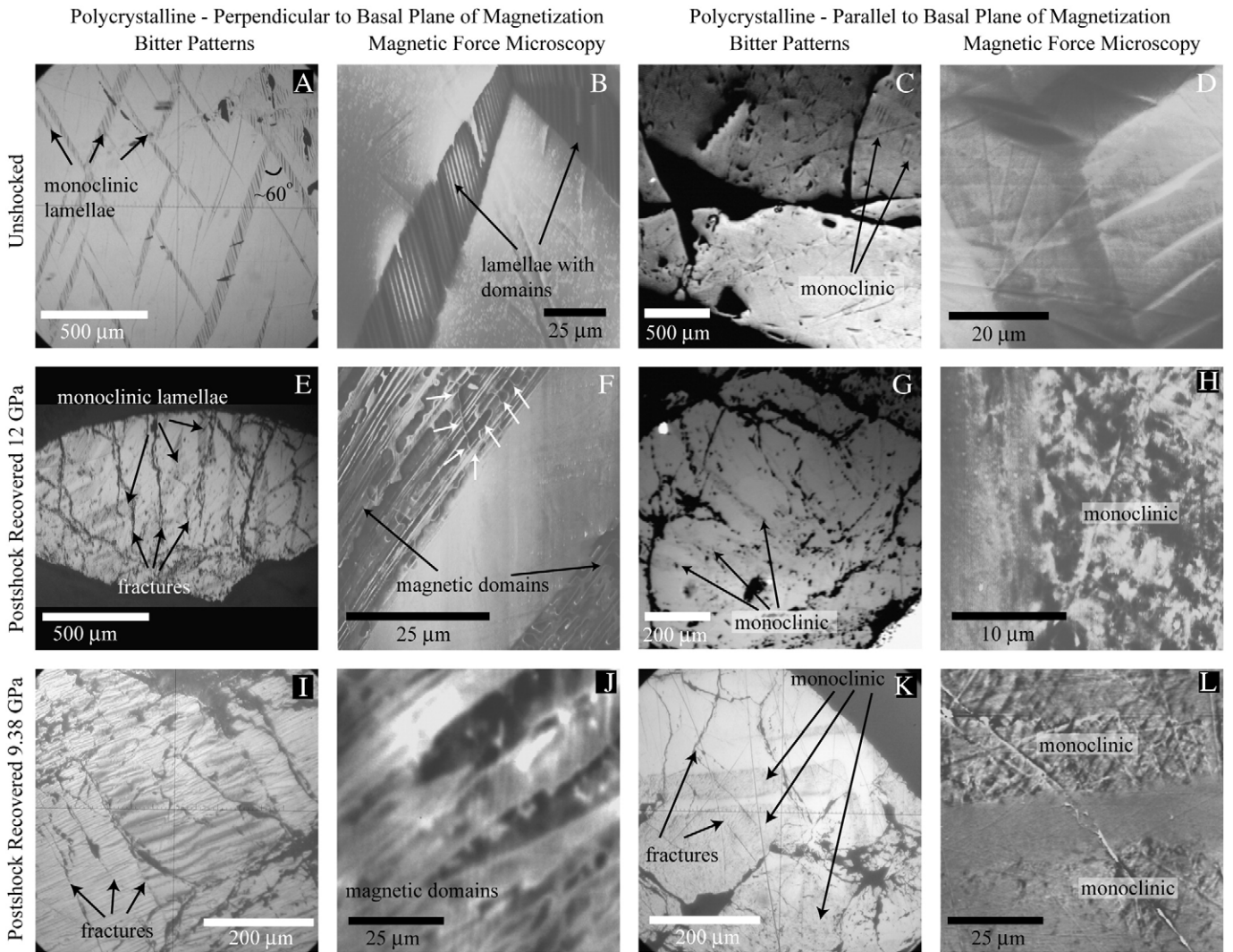


Fig. 7. Magnetic imaging of polished (0.02 μm) (A–D) unshocked and (E–L) postshock recovered MD polycrystalline pyrrhotite. Postshock samples are AF demagnetized in 85 mT peak fields. Vertical lines in (J) are an artifact of optical interference.

at altitude are up to ~ 20 times greater than terrestrial anomalies at similar altitudes (Langel et al., 1982; Acuña et al., 1999).

In the pressure range suggested to be responsible for shock demagnetization of the Martian crust around Hellas basin (Louzada and Stewart, 2009), the observed reduction of magnetization in pyrrhotite makes pyrrhotite a candidate for Mars. However, the similarity between pressure demagnetization results of different minerals precludes the exclusion of other magnetic carriers on Mars at present.

The stability of magnetic minerals at depth is controlled by the lithostatic pressure and geothermal gradient. At the base of the Martian crust, ~ 50 – 100 km depth (Zuber, 2001), the lithostatic pressure is only ~ 0.5 – 1 GPa. Based on thermal evolution models and assuming that (i) lithostatic pressure demagnetization of the Martian crust and (ii) the pressure dependence of the Curie temperature of pyrrhotite (320°C) are negligible, remanence in pyrrhotite in the Martian crust may have been stable at depths up to ~ 50 km (Arkani-Hamed, 2005) throughout Mars' history.

Since the formation of the Martian crust, the vertical extent of the magnetized layer has likely been reduced. Thermoviscous decay of remanence at depth in the absence of a global field may have raised the lower boundary of the magnetized crust (Shahnas and Arkani-Hamed, 2007). The upper boundary would have been further reduced due to the numerous impacts over Mars' history generating shock

pressures of a few GPa and partially demagnetizing the upper ~ 10 – 20 km globally (Arkani-Hamed, 2005). Secondary impacts from large basin forming events are also capable of demagnetizing the upper crust around basins greater than ~ 500 km in diameter (Artemieva et al., 2005). However, since the initial shock event should result in the greatest reduction of magnetization, the demagnetization effects of multiple overlapping impacts over time can be disregarded in this discussion.

The simultaneous shock demagnetization of the PSD schist in two perpendicular directions yields similar demagnetization values (Fig. 2B), as opposed to the strong orientation-dependent demagnetization of the pure MD polycrystalline sample. With its lower magnetic anisotropy ($P=1.74$, $T=0.70$), the PSD schist is a much better analogue of the Martian shergottites ($P=1.06 \pm 0.03$, $T=0.21$) (Gattacceca et al., 2008) and crust. We suggest that magnetic anisotropy effects can generally be ignored in the interpretation of shock demagnetization of Martian basalts.

A number of outstanding questions remain regarding the nature of the Martian magnetic crust. The magnetic mineral distribution on Mars has to satisfy both the high intensity and the pressure demagnetization of the crust. Even accounting for the observed increase in saturation remanence as a result of shock, the localized high intensity of the Martian magnetization cannot be satisfactorily explained at present. Although a strong (10 times Earth, or several hundred microteslas)

paleofield could account for this, recent analyses of the 4 Ga Martian meteorite ALH 84001 suggest that the paleofield was only of order 50 μT (Gattacceca and Rochette, 2004; Weiss et al., 2008). Since pressure preferentially removes the low coercivity fraction of magnetization (Fig. 4B and C), and isothermal remanent magnetization has a lower coercivity than thermoremanent magnetization, pressure demagnetization of the Martian basaltic crust may be less efficient than implied by our study and therefore has not been adequately quantified at present. Finally, the interpretation of the distribution of the magnetization in the Martian crust is dependent on the poorly constrained coherence scale of the magnetization, resolution limitations of the field maps, and the possible spatial distribution of magnetic minerals and intensity.

5. Conclusions

Our main conclusions are summarized here:

- Both static and dynamic compression of pyrrhotite result in preferential demagnetization of low coercivity components.
- Pressure demagnetization can be divided into a low- and a high-pressure regime approximately separated by the ferri- to paramagnetic transition in pyrrhotite at 3–4.5 GPa. This transition also coincides with the Hugoniot Elastic Limit (~ 3.5 GPa), the onset of a broad transition region along the Hugoniot to a high-pressure phase, and a change in the lattice compressibility of pyrrhotite. It is possible that the Hugoniot Elastic Limit coincides with the structural phase transition. However, more static and shock experiments are needed to determine the equation of state of pyrrhotite.
- Hydrostatic stresses in the low-pressure regime, below the Hugoniot Elastic Limit, do not induce permanent changes in the magnetic properties, probably because the pressures are too low to cause damage to the crystal structure.
- Permanent changes do occur for pyrrhotite shocked in the high-pressure regime and include increases in saturation remanence and bulk coercivity. These observations are attributed to microfracturing and pinning of domain walls, resulting in more single-domain like behavior and magnetic hardening.
- Magnetic imaging of the shocked samples reveals undulating and sinuous domain boundaries compared to simple, linear 180° domain walls in unshocked pyrrhotite.
- The changes in magnetic remanence and magnetic properties generally hold for all magnetic minerals. However, there are differences between the experimental results on pure pyrrhotite minerals and pyrrhotite-bearing rocks.
- The direction of shock with respect to magnetic anisotropy or rock fabric does not appear to be an important factor in the magnitude of demagnetization in pyrrhotite-bearing schists.
- Pressures of a few GPa are sufficient to demagnetize pyrrhotite substantially and can explain the demagnetization signatures observed around impact basins on Mars. Changes in magnetic and crystalline properties are sensitive indicators of shock and may be used to interpret the shock history of meteorites and terrestrial rocks.

Acknowledgements

Thanks to G. Kennedy (Kumamoto U.), L. Farina, W. Croft, C. Francis, R. Staples, D. Lange, F. Ilievski, P. Hedman (Harvard), M. Jackson, J. Bowles, P. Sølheid, B. Moskowitz, J. Feinburg (IRM, U. of Minnesota), J. Kirschvink, I. Hilburn, T. Raub (Caltech), D. Evans, R. Mitchell, I. Rose, Taylor Kilian (Yale), R. Kopp (Princeton), P. Rochette (CEREGE), S. Bogue (Occidental Coll.), C. Ross, V. Sivakumar (MIT), and three anonymous reviewers. K.L.L. was supported by the Amelia Earhart Fellowship (Zonta Int.) and the IRM Visiting Researcher Fellowship. This research was supported by NASA Mars Fundamental Research Program (NNG04GD17G and NNX07AQ69G).

Appendix A. Supplementary data

Supplementary data associated with this article can be found, in the online version, at doi:10.1016/j.epsl.2009.12.006.

References

- Acuña, M.H., Connerney, J.E.P., Ness, N.F., Lin, R.P., Mitchell, D., Carlson, C.W., McFadden, J., Anderson, K.A., Rème, H., Mazelle, C., Vignes, D., Wasilewski, P., Cloutier, P., 1999. Global distribution of crustal magnetization discovered by the Mars global surveyor MAG/ER experiment. *Science* 284, 790–793. doi:10.1126/science.284.5415.790.
- Ahrens, T.J., 1979. Equations of state of iron sulfide and constraints on the sulfur content of the Earth. *JGR* 84, 985–998.
- Antretter, M., Fuller, M., 2002. Paleomagnetism and rock magnetism of Martian meteorite ALH 84001. *Phys. Chem. Earth* 27, 1299–1303. doi:10.1016/S1474-7065(02)00134-1.
- Arkani-Hamed, J., 2005. Magnetic crust of Mars. *JGR* 110. doi:10.1029/2004JE002397.
- Artemieva, N., Hood, L., Ivanov, B.A., 2005. Impact demagnetization of the Martian crust: primaries versus secondaries. *GRL* 32. doi:10.1029/2005GL024385.
- Bennet, G.E.G., Graham, J., 1981. New observations on natural pyrrhotite: magnetic transition in hexagonal pyrrhotite. *Am. Mineral.* 66, 1254–1257.
- Bennet, G.E.G., Graham, J., Thorner, M.R., 1972. New observations on natural pyrrhotites – Part I. *Mineragraphic Techniques. Am. Mineral.* 57, 445–462.
- Bertaut, E.F., 1953. Contribution à l'étude des structures lacunaires: La pyrrhotine. *Acta Crystallogr.* 6, 557–561. doi:10.1107/S0365110X53001502.
- Bertelsen, P., Goetz, W., Madsen, M.B., Kinch, K.M., Hviid, S.F., Knudsen, J.M., Gunnlaugsson, H.P., Merrison, J., Nornberg, P., Squyres, S.W., Bell III, J.F., Herkenhoff, K.E., Gorevan, S., Yen, A.S., Myrick, T., Klingelhöfer, G., Rieder, R., Gellert, R., 2004. Magnetic properties experiments on the Mars exploration Rover Spirit at Gusev Crater. *Science* 305, 827–829. doi:10.1126/science.1100112.
- Bezaeva, N.S., Rochette, P., Gattacceca, J., Sadykov, R.A., Trukhin, V.I., 2007. Pressure demagnetization of the Martian crust: ground truth from SNC meteorites. *GRL* 34, L23202. doi:10.1029/2007GL031501.
- Bezaeva, N.S., Gattacceca, J., Rochette, P., Sadykov, R.A., Trukhin, V.I., in press. An overview of the demagnetization of terrestrial and extraterrestrial rocks under hydrostatic pressure up to 1.2 GPa. *PEPI*.
- Bitter, F., 1931. On inhomogeneities in the magnetization of ferromagnetic materials. *Phys. Rev.* 38, 1903–1905. doi:10.1103/PhysRev.38.1903.
- Borradaile, G.J., Jackson, M., 1993. Changes in magnetic remanence during simulated deep sedimentary burial. *PEPI* 77, 315–327.
- Cisowski, S.M., Fuller, M., 1978. The effect of shock on the magnetism of terrestrial rocks. *JGR* 83, 3441–3458.
- Collinson, D.W., 1986. Magnetic properties of Antarctic shergottite meteorites EETA 79001 and ALHA 77005: possible relevance to a Martian magnetic field. *EPSL* 77 (2), 159–164. doi:10.1016/0012-821X(86)90157-3.
- Crawford, D.A., Schultz, P.H., 1988. Laboratory observations of impact-generated magnetic fields. *Nature* 336, 50–52.
- Dekkers, M.J., 1988. Magnetic properties of natural pyrrhotite Part I: Behaviour of initial susceptibility and saturation-magnetization-related rock-magnetic parameters in a grain-size dependent framework. *PEPI* 52, 376–393.
- Dekkers, M.J., 1989. Magnetic properties of natural pyrrhotite. II High- and low-temperature behaviour of Jrs and TRM as function of grain size. *PEPI* 57, 266–283.
- Dekkers, M.J., Mattei, J.L., Fillion, G., Rochette, P., 1989. Grain-size dependence of the magnetic-behavior of pyrrhotite during its low-temperature transition at 34-K. *GRL* 16, 855–858.
- Dunlop, D.J., Arkani-Hamed, J., 2005. Magnetic minerals in the Martian crust. *JGR* 110, E12S04. doi:10.1029/2005JE002404.
- Dunlop, D.J., Özdemir, Ö., 1997. *Rock Magnetism – Fundamentals and Frontiers*. Cambridge University Press, Cambridge.
- Fleet, M.E., 1968. On the lattice parameters and superstructures of pyrrhotites. *Am. Mineral.* 53, 1846–1855.
- Frey, H., 2008. Ages of very large impact basins on Mars: implications for the late heavy bombardment in the inner solar system. *GRL* 35, L13203. doi:10.1029/2008GL033515.
- Gattacceca, J., Rochette, P., 2004. Toward a robust normalized magnetic paleointensity method applied to meteorites. *EPSL* 227, 377–393.
- Gattacceca, J., Berthe, L., Boustie, M., Vadeboin, F., Rochette, P., De Resseguier, T., 2007a. On the efficiency of shock remanent processes. *PEPI*. doi:10.1016/j.pepi.2007.1009.1005.
- Gattacceca, J., Lamali, A., Rochette, P., Boustie, M., Berthe, L., 2007b. The effects of explosive-driven shocks on the natural remanent magnetization and the magnetic properties of rocks. *PEPI* 162, 85–98. doi:10.1016/j.pepi.2007.1003.1006.
- Gattacceca, J., Rochette, P., Gounelle, M., Van Ginneken, M., 2008. Magnetic anisotropy of HED and Martian meteorites and implications for the crust of Vesta and Mars. *EPSL* 270 (3–4), 280–289. doi:10.1016/j.epsl.2008.03.047.
- Gilder, S.A., Le Goff, M., 2008. Systematic pressure enhancement of titanomagnetite magnetization. *GRL* 35, L10302. doi:10.1029/2008GL033325.
- Gilder, S.A., LeGoff, M., Chervin, J.-C., Peyronneau, J., 2004. Magnetic properties of single and multi-domain magnetite under pressures from 0 to 6 GPa. *GRL* 31 (10). doi:10.1029/2004GL019844.
- Gilder, S.A., Le Goff, M., Chervin, J.-C., 2006. Static stress demagnetization of single and multi-domain magnetite with implications for meteorite impacts. *High Pressure Res.* 26 (4), 539–547. doi:10.1080/08957950601092085.
- Halgedahl, S.L., Fuller, M., 1981. The dependence of magnetic domain structure upon magnetization state in polycrystalline pyrrhotite. *PEPI* 26, 93–97.

- Halgedahl, S., Ye, J., 2000. Observed effects of mechanical grain-size reduction on the domain structure of pyrrhotite. *EPSL* 176, 457–467.
- Hood, L.L., Richmond, N.C., Pierazzo, E., Rochette, P., 2003. Distribution of crustal magnetic fields on Mars: shock effects of basin-forming impacts. *GRL* 30, 1281–1284. doi:10.1029/2002GL016657.
- Hrouda, F., 2007. Anisotropy of magnetic susceptibility of rocks in the Rayleigh Law region: modelling errors arising from linear fit to non-linear data. *Stud. Geophys. Geod.* 51, 423–438. doi:10.1007/s11200-007-0024-5.
- Jackson, M., Borradaile, G., Hudleston, P., Banerjee, S., 1993. Experimental deformation of synthetic magnetite-bearing calcite sandstones: effects on remanence, bulk magnetic properties, and magnetic anisotropy. *JGR* 98 (B1), 383–401.
- Jelinek, V., 1973. Precision A.C. bridge set for measuring magnetic susceptibility of rocks and its anisotropy. *Stud. Geophys. Geod.* 17, 36–48. doi:10.1007/BF01614027.
- Kamimura, T., Sato, M., Takahashi, H., Mori, N., Yoshida, H., Kaneko, T., 1992. Pressure-induced phase transition in Fe–Se and Fe–S systems with a NiAs-type structure. *J. Magn. Magn. Miner.* 104–107, 255–256. doi:10.1016/0304-8853(92)90787-O.
- Kinoshita, H., 1968. Studies on piezo-magnetization (III)-PRM and relating phenomena. *J. Geomagn. Geoelectr.* 20 (3), 155–167.
- Kirichenko, A.S., Kornilov, A.V., Pudalov, V.M., 2005. Properties of polyethylsiloxane as a pressure-transmitting medium. *Instrum. Exp. Tech.* 48 (6), 813–816. doi:10.1007/s10786-005-0144-5.
- Kletetschka, G., Connerney, J.E.P., Ness, N.F., Acuña, M.H., 2004. Pressure effects on martian crustal magnetization near large impact basins. *MAPS* 39, 1839–1848.
- Kobayashi, H., Sato, M., Kamimura, T., Sakai, M., Onodera, H., Kuroda, N., Yamaguchi, Y., 1997. The effect of pressure on the electronic states of FeS and Fe₇S₈ studied by Mössbauer spectroscopy. *J. Phys. Condens. Matter* 9, 515–527. doi:10.1088/0953-8984/9/2/019.
- Kontny, A., de Wall, H., Sharp, T.G., Pósfai, M., 2000. Mineralogy and magnetic behavior of pyrrhotite from a 260 C section at the KTB drilling site, Germany. *Am. Mineral.* 85, 1416–1427.
- Kontny, A., Elbra, T., Just, J., Pesonen, L.J., Schleicher, A.M., Zolk, J., 2007. Petrography and shock-related remagnetization of pyrrhotite in drill cores from the Bosumtwi Impact Crater Drilling Project, Ghana. *MAPS* 42 (4/5), 811–827.
- Langel, R.A., Phillips, J.D., Horner, R.J., 1982. Initial scalar magnetic anomaly map from MAGSAT. *GRL* 9 (4), 269–272.
- Lillis, R.J., Mitchell, D.L., Lin, R.P., Connerney, J.E.P., Acuña, M.H., 2004. Mapping crustal magnetic fields at Mars using electron reflectometry. *GRL* 31. doi:10.1029/2004GL020189.
- Lillis, R.J., Frey, H.V., Manga, M., 2008a. Rapid decrease in Martian crustal magnetization in the Noachian era: implications for the dynamo and climate of early Mars. *GRL* 35, L14203. doi:10.1029/2008GL034338.
- Lillis, R.J., Frey, H.V., Manga, M., Mitchell, D.L., Lin, R.P., Acuña, M.H., Bougher, S.W., 2008b. An improved crustal magnetic field map of Mars from electron reflectometry: highland volcano magmatic history and the end of the martian dynamo. *Icarus* 194, 575–596. doi:10.1016/j.icarus.2007.09.032.
- Longhi, J., Knittle, E., Holloway, J.R., Wänke, H., 1992. 6. The bulk composition, mineralogy and internal structure of Mars. In: Kieffer, H.H., Jakosky, B.M., Snyder, C.W., Matthews, M.S. (Eds.), *Mars*. The University of Arizona Press, Tucson, pp. 184–208.
- Louzada, K.L., Stewart, S.T., 2009. Effects of planet curvature and crust on the shock pressure field around impact basins. *GRL* 36, L15203. doi:10.1029/2009GL037869.
- Louzada, K.L., Stewart, S.T., Weiss, B.P., 2007. Effect of shock on the magnetic properties of pyrrhotite, the Martian crust, and meteorites. *GRL* 34, L05204. doi:10.1029/2006GL027685.
- Louzada, K.L., Weiss, B.P., Maloof, A.C., Stewart, S.T., Swanson-Hysell, N.L., Soule, S.A., 2008. Paleomagnetism of Lomar impact crater, India. *EPSL* 275 (3–4), 308–319. doi:10.1016/j.epsl.2008.08.025.
- Martín-Hernández, F., Dekkers, M.J., Bominaar-Silkens, I.M.A., Maan, J.C., 2008. Magnetic anisotropy behaviour of pyrrhotite as determined by low- and high-field experiments. *GJI* 174, 42–54. doi:10.1111/j.1365-246X.2008.03793.x.
- McSween Jr, H.Y., Treiman, A.H., 1998. Chapter 6: Martian meteorites. In: Papike, J.J. (Ed.), *Planetary Materials*, p. 53.
- Melosh, H.J., 1989. *Impact Cratering: A Geologic Process*. Oxford University Press, New York.
- Menyeh, A., O'Reilly, W., 1991. The magnetization process in monoclinic pyrrhotite (Fe₇S₈) particles containing few domains. *GJI* 104 (2), 387–399.
- Mohit, P.S., Arkani-Hamed, J., 2004. Impact demagnetization of the martian crust. *Icarus* 168, 305–317. doi:10.1016/j.icarus.2003.12.005.
- Morimoto, N., Gyobu, A., Tsukuma, K., Koto, K., 1975. Superstructure and nonstoichiometry of intermediate pyrrhotite. *Am. Mineral.* 60 (3–4), 240–248.
- Nagata, T., 1966. Main characteristics of piezo-magnetization and their qualitative interpretation. *J. Geomagn. Geoelectr.* 18 (1), 81–97.
- Nagata, T., 1971. Introductory notes on shock remanent magnetization and shock demagnetization of igneous rocks. *Pure Appl. Geophys.* 89, 159–177.
- Nagata, T., Carleton, B.J., 1969. Notes on piezo-remanent magnetization of igneous rocks II. *J. Geomagn. Geoelectr.* 21 (1), 427–445.
- Nagata, T., Kinoshita, H., 1964. Effect of release of compression on magnetization of rocks and assemblies of magnetic minerals. *Nature* 204, 1183–1184.
- Nagata, T., Kinoshita, H., 1967. Effect of hydrostatic pressure on magnetostriction and magnetocrystalline anisotropy of magnetite. *PEPI* 1, 44–48.
- Nkoma, J.S., Ekosse, G., 1999. X-ray diffraction of chalcopyrite CuFeS₂, pentlandite (Fe, Ni)₉S₈ and pyrrhotite Fe_{1–x}S₈ obtained from Cu–Ni ore bodies. *J. Phys. Condens. Matter* 11, 121–128.
- Pohl, J., Bleil, U., Hornemann, U., 1975. Shock magnetization and demagnetization of basalt by transient stress up to 10 kbar. *J. Geophys.* 41, 23–41.
- Pósfai, M., Sharp, T.G., Kontny, A., 2000. Pyrrhotite varieties from the 9.1 km deep borehole of the KTB project. *Am. Mineral.* 85, 1406–1415.
- Rochette, P., Mattéi, J.-L., Dekkers, M.J., 1990. Magnetic transition at 30–34 Kelvin in pyrrhotite: insight into a widespread occurrence of this mineral in rocks. *EPSL* 98, 319–328.
- Rochette, P., Lorand, J.-P., Fillion, G., Sautter, V., 2001. Pyrrhotite and the remanent magnetization of SNC meteorites: a changing perspective of Martian magnetism. *EPSL* 190, 1–12.
- Rochette, P., Fillion, G., Ballou, R., Brunet, F., Ouladdiaf, B., Hood, L., 2003. High pressure magnetic transition in pyrrhotite and impact demagnetization on Mars. *GRL* 30. doi:10.1029/2003GL017359.
- Rochette, P., Gattacceca, J., Chevrier, V., Hoffmann, V., Lorand, J.-P., Funaki, M., Hochleitner, R., 2005. Matching Martian crustal magnetization and magnetic properties of Martian meteorites. *MAPS* 40, 529–540.
- Sadykov, R.A., Bezaeva, N.S., Kharkovskiy, A.I., Rochette, P., Gattacceca, J., Trukhin, V.I., 2008. Nonmagnetic high pressure cell for magnetic remanence measurements up to 1.5 GPa in a superconducting quantum interference device magnetometer. *Rev. Sci. Instrum.* 79 (11), 115102. doi:10.1063/1.2999578.
- Sekine, T., Kobayashi, T., Nishio, M., Takahashi, E., 2008. Shock equation of state of basalt. *Earth Planets and Space* 60 (9), 999–1003.
- Shahnas, H., Arkani-Hamed, J., 2007. Viscous and impact demagnetization of Martian crust. *JGR* 112 (E02009). doi:10.1029/2005JE002424.
- Soffel, H., 1977. Pseudo-single-domain effects and single domain-multidomain transition in natural pyrrhotite deduced from domain-structure observations. *J. Geophys.* 42 (4), 351–359.
- Soffel, H.C., 1981. Domain structure of natural fine-grained pyrrhotite in a rock matrix (diabase). *PEPI* 26, 98–106. doi:10.1016/0031-9201(81)90102-3.
- Stewart, S.T., 2004. The shock compression laboratory at Harvard: a new facility for planetary impact processes. *Lunar and Planetary Science*, vol. XXXV. Lunar and Planetary Institute, Houston, TX. p. Abs. No. 1290.
- Vaughan, D.J., Tossell, J.A., 1973. Magnetic transitions observed in sulfide minerals at elevated pressures and their geophysical significance. *Science* 179, 375–377. doi:10.1126/science.179.4071.375.
- Weiss, B.P., Vali, H., Baudenbacher, F.J., Kirschvink, J.L., Stewart, S.T., Shuster, D.L., 2002. Records of an ancient Martian magnetic field in ALH84001. *EPSL* 201, 449–463.
- Weiss, B.P., Fong, L.E., Vali, H., Lima, E.A., Baudenbacher, F.J., 2008. Paleointensity of the ancient Martian magnetic field. *GRL* 35, L23207. doi:10.1029/2008GL035585.
- Yund, R.A., Hall, H.T., 1969. Hexagonal and monoclinic pyrrhotites. *Econ. Geol.* 64, 420–423.
- Zuber, M.T., 2001. The crust and mantle of Mars. *Nature* 412, 220–227. doi:10.1038/35084163.

Shock and Static Pressure Demagnetization of Pyrrhotite and Implications for the Martian Crust

- Supplemental material -

Karin L. Louzada^{1,2*}, Sarah T. Stewart², Benjamin P. Weiss³, Jérôme Gattacceca⁴, Natalia S.
Bezaeva⁵

¹Netherlands Office for Science and Technology, Royal Netherlands Embassy, 4200 Linnean
Avenue, NW, Washington, D.C. 20008, USA

²Department of Earth and Planetary Sciences, Harvard University, 20 Oxford Street, Cambridge,
MA 02138, USA

³Department of Earth, Atmospheric and Planetary Sciences, Massachusetts Institute of
Technology 54-814, 77 Massachusetts Avenue, Cambridge, MA 02139, USA

⁴Department of Geophysics and Planetology, CEREGE (CNRS, Aix-Marseille University), BP
80, 13545 Aix en Provence Cedex 4, France

⁵Earth Physics Department, Faculty of Physics, M.V. Lomonosov Moscow State University,
Leninskie gory, 119991, Moscow, Russia

*louzada@post.harvard.edu

Contents:

	<i>Figure</i>	<i>Table</i>	<i>Page</i>
1. X-ray diffraction	Figure S1	Table S1	2
2. Chemical composition		Table S2	4
3. Magnetic hysteresis		Table S3	5
4. Anisotropy of magnetic susceptibility	Figure S2	Table S4	7
5. Experimental setup for shock experiments	Figure S3		9
6. Pressure distribution in the shocked samples	Figure S4		10
7. Impedance match solution		Table S5	11
8. Hugoniot Elastic Limit	Figure S5	Table S6	12
9. Photomicrographs of shocked pyrrhotite	Figure S6		14
10. Domain interactions	Figure S7		15
11. Magnetic imaging of pyrrhotite nodule	Figure S8		16
12. References			17

Citation: Louzada, K.L., et al., Shock and static pressure demagnetization of pyrrhotite and implications
for the Martian crust, Earth Planet. Sci. Lett. (2009), doi:10.1016/j.epsl.2009.12.006

1. X-ray diffraction

X-ray diffraction patterns were obtained for powdered samples using the Scintag XDS2000 fixed sample position powder diffractometer between 2 and 70° (2 θ) at Harvard University. D-spacing values of peaks identified with known indices of pyrrhotite are shown in Table S1. Two additional weak peaks were detected at 2.8483 – 2.8643 Å and 1.5968 – 1.6096 Å, respectively. The latter peak could be related to the (312) plane in chalcopyrite (CuFeS₂), which may occur as small inclusions in natural pyrrhotite. However, Cu was not measured in the microprobe analyses (Table S2) and therefore this interpretation cannot be independently confirmed. Lattice parameters, *a* and *c*, were determined for a hexagonal lattice using the technique described in Nkoma and Ekosse (1999) and are consistent with previous pyrrhotite measurements (Dekkers, 1988; Nkoma and Ekosse, 1999). Monoclinic pyrrhotite was independently observed by a doublet at [208]. Thanks to W. Croft, Harvard University.

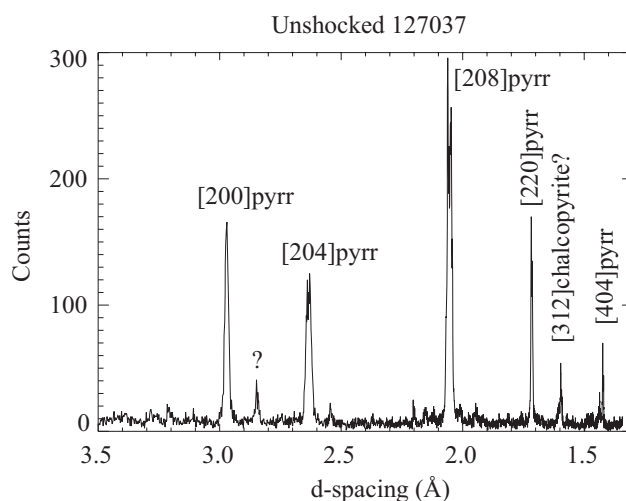


Figure S1 Example X-ray diffraction pattern for unshocked polycrystalline pyrrhotite.

Table S1 X-ray diffraction results

<i>d-spacing</i>	<i>Unshocked</i>	
	<i>Nodule (No. 98080)</i>	<i>Polycrystalline (No. 127037)</i>
$d_{(200)}$ (Å)	2.9737 (0.0058) ^a	2.9703
$d_{(204)}$ (Å)	2.6421 (0.0025) ^a	2.6300
$d_{(208)}$ (Å)	2.0642 (0.0025) ^a	2.0615, 2.0473 ^c
$d_{(220)}$ (Å)	1.7184 (0.0021) ^a	1.7179
$d_{(404)}$ (Å)	1.4324 (0.0005) ^b	1.4238
a (Å)	6.875 (0.006)	6.846 (0.033)
c (Å)	22.89 (0.06)	22.84 (0.23)
	<i>Postshock</i>	
	<i>Nodule (98080-1D) (5.67 GPa)</i>	<i>Polycrystalline (127037-A) (6.92 GPa)</i>
$d_{(200)}$ (Å)	2.9839	2.9800
$d_{(204)}$ (Å)	2.6436	2.6436
$d_{(208)}$ (Å)	2.0669	2.0669
$d_{(220)}$ (Å)	1.7215	1.7227
$d_{(404)}$ (Å)	1.4304	
a (Å)	6.874 (0.028)	6.884 (0.005)
c (Å)	22.94 (0.12)	22.91 (0.06)

^{a,b} Average of three ^(a), two ^(b) measurements. ^c Split peak indicative of monoclinic pyrrhoite. 1 σ errors are indicated in parentheses.

2. Chemical composition

Spot microprobe chemical composition analyses were performed using the Camica Electron Microprobe at Harvard University. Operating conditions were 15 keV and 30.17 nA, with a beam size of 8 μm . Thanks to David Lange, Harvard University.

Table S2 Averaged (1σ) atom percentage chemical composition of pyrrhotite samples

<i>Element</i>	<i>Nodule (No. 98080)</i>	<i>Polycrystalline (No. 127037)</i>
S	52.70 (0.34)	53.29 (0.18)
Fe	47.07 (0.23)	46.70 (0.17)
Mn	b.d.l.	b.d.l.
Co	0.056 (0.007)	0.022 (0.005)
Ni	0.226 (0.050)	b.d.l.
Zn	b.d.l.	b.d.l.
Total	100.13	100.17
Fe/S	0.893 (0.01)	0.876 (0.01)
Number of measurements	11	26

b.d.l. = below detection limit

3. Magnetic hysteresis

Unshocked pyrrhotite magnetic hysteresis measurements (Table S3) were performed on the Micromag Vibrating Sample Magnetometer with ± 1 T maximum field at CEREGE, France. Postshock pyrrhotite magnetic hysteresis measurements were performed on the Micromag Vibrating Sample Magnetometer at the Institute for Rock Magnetism, University of Minnesota with maximum field ± 1.8 T. Due to variable monoclinic to hexagonal pyrrhotite distributions in the samples and the small sample masses direct comparison of the saturation moment (M_s) and saturation remanence (M_{rs}) cannot be made between the unshocked and shocked samples in this table. However, M_{rs}/M_s comparisons are meaningful indicators of relative differences in grain size. Thanks to M. Jackson and J. Bowles at IRM, University of Minnesota.

Table S3 Magnetic hysteresis results

<i>Hysteresis</i>		<i>Unshocked</i>						
<i>Parameter</i> (1σ)	<i>Nodule</i> (No. 98080) ^a	<i>Polycrystalline</i> (No. 127037) ^a		<i>Schist</i> ^b				
M_s (Am ² /kg)	1.130 (0.027) × 10 ⁻³	1.405 (0.029) × 10 ⁻²		9.14 (6.02) × 10 ⁻²				
M_{rs} (Am ² /kg)	5.644 (0.022) × 10 ⁻⁴	2.089 (0.022) × 10 ⁻³		4.48 (2.90) × 10 ⁻²				
M_{rs}/M_s	0.4991 (0.010)	0.1487 (0.004)		0.499 (0.028)				
B_c (mT)	5.507 (0.449)	4.643 (0.028)		23.8 (5.9)				
B_{cr} (mT)	5.481 (0.552)	7.001 (0.075)		31.3 (11.7)				
B_{cr}/B_c	0.9941 (0.0224)	1.508 (0.012)		1.29 (0.12)				
mass (mg)	9.7	11.2		173.2-364.7 (n=10)				
Domain size	SD/SP	MD		PSD				
<i>Postshock</i> ^c								
	<i>Nodule</i>			<i>Polycrystalline</i>				
<i>Parameter</i>	<i>98080-1L</i>	<i>98080-1K</i>	<i>98080-1H</i>	<i>98080-1A</i>	<i>127037-G</i>	<i>127037-D</i>	<i>127037-L</i> ^d	<i>127037-N*</i>
(RMSres/RMSdata)	(1.74 GPa)	(2.81 GPa)	(2.89 GPa)	(3.3 GPa)	(0.99 GPa)	(5.67 GPa)	(9.83 GPa)	(9.83 GPa)
M_s (× 10 ⁻³ Am ² /kg)	0.705 (0.02)	1.415 (0.07)	2.777 (0.86)	0.9217 (0.06)	1.065 (0.12)	4.329 (0.39)		15.95 (0.79)
M_{rs} (× 10 ⁻³ Am ² /kg)	0.374 (0.03)	0.720 (0.06)	1.186 (0.30)	0.4538 (0.05)	0.330 (0.04)	2.022 (0.22)		7.698 (0.54)
M_{rs}/M_s	0.454 (0.06)	0.4266 (0.05)	0.4634 (0.15)	0.4412 (0.07)	0.317 (0.08)	0.4635 (0.04)	0.5527 (0.10)	0.4722 (0.02)
B_c (mT)	8.816 (2.03)	18.37 (2.76)	15.26 (8.70)	9.739 (2.82)		24.08 (10.59)	18.65 (7.65)	46.11 (5.53)
mass (mg)	1.2	12.0	17.3	1.9	1.3	9.2	<0.6	1.8

M_s = saturation magnetization (corrected for paramagnetic contribution), M_{rs} = saturation remanence, B_c = coercivity, B_{cr} = coercivity of remanence.

^a Average hysteresis parameters (1σ) of measurements made in three perpendicular orientations. ^b Hysteresis parameters reported in Gattacceca, et al. (2007). ^c

Geometric mean ($\sqrt[3]{\kappa_1 \cdot \kappa_2 \cdot \kappa_3}$) of ellipsoids fit to the hysteresis parameters measured in 12 orientations, where κ_1 , κ_2 and κ_3 are the principal axes of the fitted ellipsoid. ^d Uncertain mass. * Shock direction is parallel to the easy plane of magnetization.

4. Anisotropy of magnetic susceptibility

The anisotropy of magnetic susceptibility (AMS) of pure pyrrhotite is field dependent (e.g., Martín-Hernández, et al., 2008) and our measurements using a Geofyzika KLY-2 KappaBridge AC Susceptibility Bridge with ac fields of 300 A/m at 920 Hz yielded erroneous results. Therefore, we determined AMS from 27 hysteresis loops in 12 directions obtained on the Princeton Measurements Vibrating Sample Magnetometer at the Institute for Rock Magnetism, University of Minnesota, with maximum field ± 1.8 T. Low field susceptibility was determined from linear slopes fit to the data between -2.5 and +2.5 mT. We then solved for the susceptibility ellipsoid using the method described in Jelínek (1973) and Coe (1966).

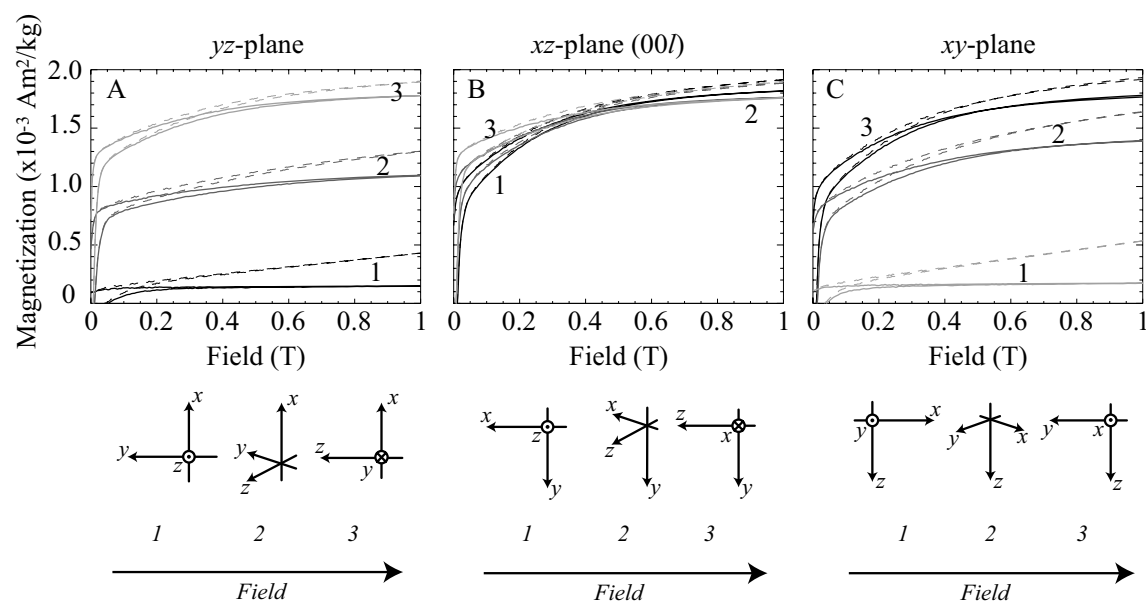


Figure S2 Partial hysteresis loops for the unshocked polycrystalline pyrrhotite (No. 127037) in three different orientations (1, 2 and 3). The inducing field is always oriented to the right and is confined to the yz-, xz- and xy-plane of the sample in panels **A**, **B** and **C**, respectively. (Right-handed coordinate system.) The xz-plane is parallel to the (00 \bar{l}) basal-plane. The oblate shape of the anisotropy is evident from the hysteresis loops in the xz-plane. Dashed lines are raw loops, solid lines are loops corrected for paramagnetic signal (linear fit between 1.5 and 1.6 T).

Table S4 Magnetic anisotropy results

<i>AMS</i>	<i>Unshocked</i>							
	<i>Nodule (No. 98080)</i>			<i>Polycrystalline (No. 127037)</i>			<i>Schist^a</i>	
<i>P</i>	45.98			56.24			1.741	
<i>L</i>	29.97			2.202			1.087	
<i>F</i>	1.534			25.53			1.601	
<i>P'</i>	66.37			71.58			1.819	
<i>T</i>	-0.776			0.608			0.697	
RMS(res)/RMS(data)	0.25			0.03				
	<i>Postshock</i>							
	<i>Nodule</i>			<i>Polycrystalline</i>				
	<i>98080-1L^a</i> <i>(1.74 GPa)</i>	<i>98080-1K</i> <i>(2.81 GPa)</i>	<i>98080-1H</i> <i>(2.89 GPa)</i>	<i>98080-1A</i> <i>(3.3 GPa)</i>	<i>127037-G</i> <i>(0.99 GPa)</i>	<i>127037-D</i> <i>(5.67 GPa)</i>	<i>127037-L</i> <i>(9.83 GPa)</i>	<i>127037-N*</i> <i>(9.83 GPa)</i>
<i>P</i>	21.96	22.79	5.448	46.46	64.38	253.9	14.20	60.62
<i>L</i>	17.12	4.684	2.410	5.285	1.505	1.375	8.626	1.181
<i>F</i>	1.211	4.865	2.260	8.791	42.77	1984.5	1.646	51.36
<i>P'</i>	31.87	22.79	5.450	46.98	98.62	501.5	16.78	104.2
<i>T</i>	-0.8757	0.0120	-0.0380	0.1325	0.803	0.884	-0.624	0.918
RMS(res)/RMS(data)	0.09	0.11	0.16	0.11	0.07	0.02	0.33	0.08

P = anisotropy degree (κ_1/κ_3), *L* = lineation (κ_1/κ_2), *F* = foliation (κ_2/κ_3), *P'* = corrected anisotropy degree ($P' = \exp\sqrt{2[(\eta_1-\eta)^2+(\eta_2-\eta)^2+(\eta_3-\eta)^2]}$), where $\eta_i = \ln(\kappa_i)$ and $\eta = (\eta_1+\eta_2+\eta_3)/3$, *T* = shape factor ($T = (2\eta_2-\eta_1-\eta_3)/(\eta_1-\eta_3)$). For a discussion on anisotropy see Jelínek (1981). ^a Measurement performed on the Geofyzika KLY-2 KappaBridge AC Susceptibility Bridge with ac field of 300 A/m and 920 Hz by M. Jackson and J. Bowles at IRM, UMN. * Shock direction is parallel to the easy plane of magnetization. ^b Low field susceptibility (± 3 mT). RMS = root mean squared. The lower RMS (res)/RMS (data), the better the fit.

5. Experimental Setup Shock Experiments

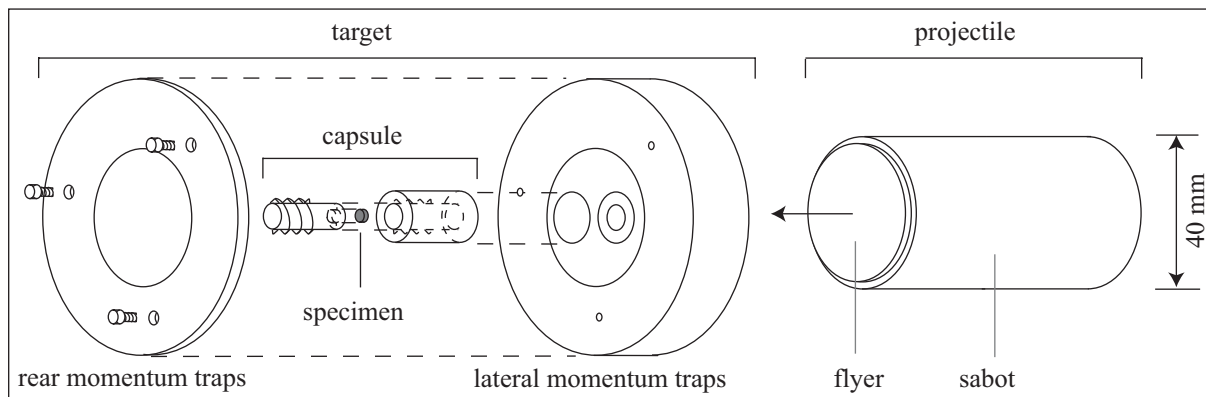


Figure S3 Example schematic diagram of an aluminum target configuration for a shock recovery experiment. Other configurations have a single capsule placed off-center. The inner capsule is smaller than the inner diameter of the 2G magnetometer. The disc-shaped specimens (3-12 mm diameter \times <1 mm thick) are positioned approximately 1.5 mm from the impact surface. Self-shorting gauges attached to the impact side of the target assembly record the tilt of the projectile (generally <10 mrad). Redundant impact velocity measurements are performed by shorting pins and lasers placed in the path of the projectile prior to impact. The impact occurs in vacuum (<100 mtorr) at room temperature in the ambient magnetic field. The target assembly is decelerated and recovered downrange in a rag-filled catch tank.

6. Pressure distribution in the samples

Our CTH (McGlaun, et al., 1990) simulations of the shock experiments on pyrrhotite indicate that 74 and 94 vol% of the specimen experiences a maximum pressure within 0.5 GPa (13%) and 1.5 GPa (38%) of the calculated peak shock pressure, respectively.

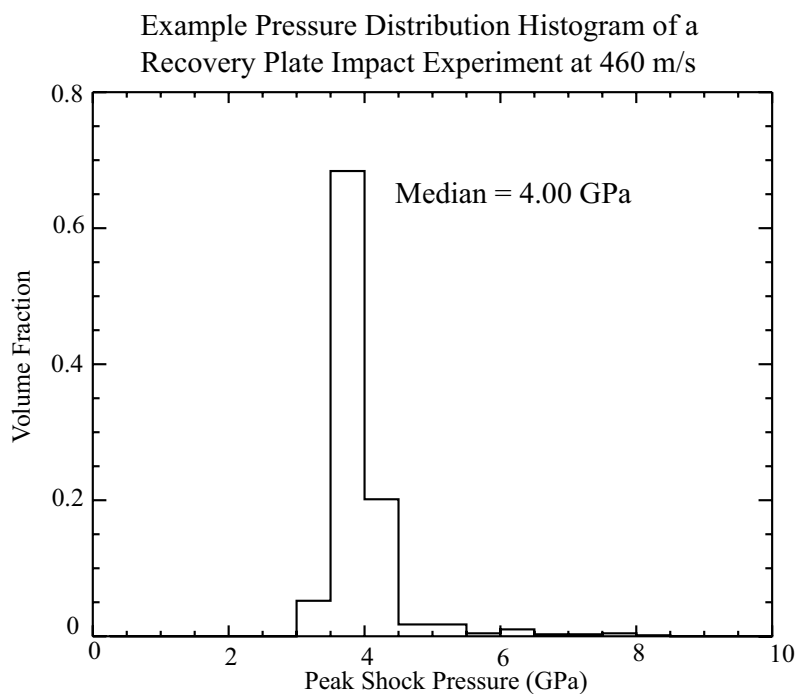


Figure S4 Histogram of the simulated pressure distribution as a function of sample volume in a pyrrhotite specimen at 460 m/s.

7. Impedance match solution

Principal stress in the shock experiments is determined using the impedance match solution, or planar impact approximation (e.g. Boslough and Asay, 1993; Melosh, 1989 p. 54-57), and the material shock parameters in Table S5. In the impedance match solution the impact is assumed to be between two infinite plates, reducing the problem to one dimension. At impact, the pressure in both the projectile (aluminum) and the target (specimen) must equal. Particle velocity and pressure (principal stress) are related to each other by the Hugoniot equation:

$\sigma_1 = P_0 + \rho_0 U_s u_p$, where σ_1 is principal stress, P_0 is the initial pressure (~ 0), ρ_0 is the initial uncompressed density, and U_s and u_p are the shock and particle velocities in km/s, respectively. U_s and u_p are related to each other via the empirical relationship:

$U_s = C + s \cdot u_p$, where C is the material specific bulk sound speed in km/s and s is the material specific dimensionless slope (Table S5). The planar impact approximation neglects attenuation of the shock wave and rarefactions that travel inward from the sides of the projectile. Errors in the shock pressure determination result from errors in the impact velocity measurement. Reflections from edge effects from the flyer will be slightly greater in the Wilson schist specimens as they are larger than the other specimens (12 mm, as opposed to 3 mm, in diameter). For the schist experiments we assume that the pressure in the specimen is equal to that in the aluminum, as their density and sound speeds are similar.

Table S5 Impedance match parameters

<i>Material</i>	<i>Uncompressed density (g/cm³)</i>	<i>C (km/s)</i>	<i>S</i>	<i>Source</i>
Al-6061	2.703	5.33 (0.04)	1.34 (0.01)	fit to data between 0 and 3.8 km/s u_p ($n = 105$) (Marsh, 1980)
Al-2024	2.784 (0.008)	5.38 (0.02)	1.27 (0.02)	fit to data between 0 and 1.3 km/s u_p ($n = 26$) (Marsh, 1980)
Pyrrhotite	4.603 (0.003)	$U_s = 4.543$ (0.005) km/s		low pressure phase (elastic shock) weighted mean ($n = 4$) (Ahrens, 1979)
Schist	2.7515 (0.0255)	see Al-2024		mean ($n = 4$) (Table 2, main text)

1 σ uncertainties are given in parentheses following mean values.

8. Hugoniot Elastic Limit

Two shock experiments to determine the Hugoniot Elastic Limit (HEL) of the solid polycrystalline pyrrhotite (No. 127037) were conducted in two perpendicular directions, parallel and perpendicular to the easy plane of magnetization (basal plane) at ~ 1150 m/s. Free surface velocities were determined simultaneously on the aluminum driver (1.2 mm thick) and a ~ 2 mm thick pyrrhotite specimen glued to the downrange side of the aluminum, using a Velocity Interferometer System for Any Reflector (Valyn-VISAR, Barker and Hollenbach, 1972). Shock velocity (U_s) in the pyrrhotite was determined from the break-out time difference of the VISAR traces on the driver and pyrrhotite sample (not shown). The experiment perpendicular to (00 l) (solid line) shows a clear two wave structure with a plateau at ~ 300 m/s indicative of the elastic precursor. Based on CTH simulations, the pressure in the first wave (the HEL) is approximately 3.5 GPa, close to the pressure determined using the particle velocity doubling rule (~ 3 GPa; e.g., Boslough and Asay, 1993, p.32). Note that the peak measured particle velocity is approximately 50 m/s less than that predicted using the impedance match solution (Table S5). Velocity measurements parallel to (00 l) (dashed line) do not show a clear two-wave structure.

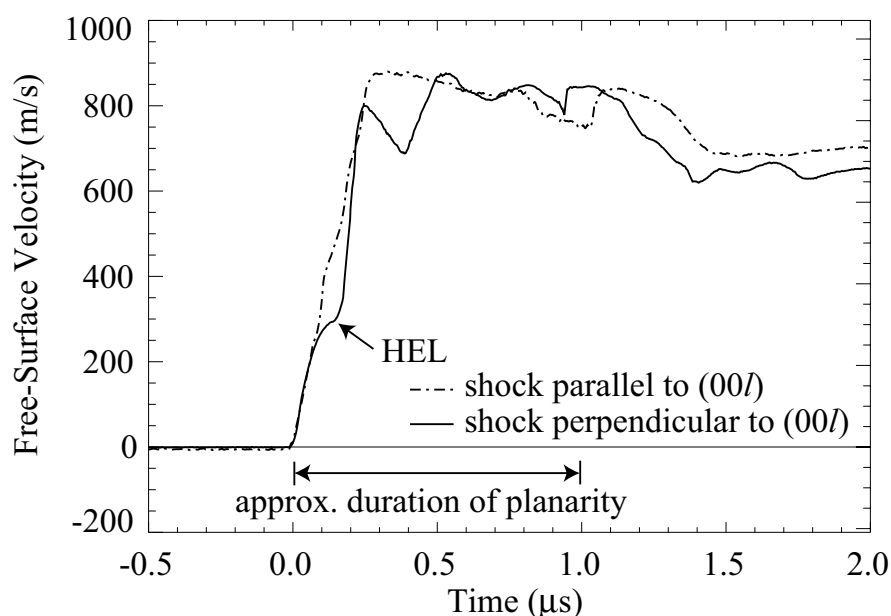


Figure S5 Free-surface laser velocity interferometry results for pyrrhotite specimens. Solid line = shock direction perpendicular to the basal plane of pyrrhotite (00 l). Dashed line = shock direction parallel to (00 l), indicated by * in other plots and tables throughout this work. HEL = Hugoniot Elastic Limit.

Table S6 Hugoniot experiment specifics

<i>Specimen Name</i>	<i>Specimen Mass (g)</i>	<i>Specimen thickness (mm)</i>	<i>Specimen density (g/cm³)</i>	c_p (m/s)	c_s (m/s)	ν	v_i (m/s)	<i>Tilt</i> (mrad)	u_p (m/s)	σ_I (GPa)	P (GPa)	U_s (km/s)	<i>HEL</i> (GPa)
12-C	2.147 (0.0017)	1.9228 (0.0062)	4.5724 (0.0173)	5.034 (0.082)	2.706 (0.025)	0.29	1156 (53.6)	0.36 (0.03)	505 (-24.3/+25.0)	10.8 (-0.53/+0.53)	6.54	-	
12-A*	1.786 (0.0017)	2.0984 (0.0072)	4.6074 (0.0081)	4.887 (0.059)	2.882 (0.021)	0.23	1171 (7.25)	3.77 (6.52)	511 (-2.4/+3.0)	10.9 (-0.08/+0.07)	5.80	4.81 (0.33)	~3.5

c_p and c_s = longitudinal and shear wave speeds. ν = Poisson's ratio. v_i = measured impact velocity. U_s = measured shock velocity. *HEL* = Hugoniot Elastic Limit. u_p = calculated particle velocity. σ_I = calculated principal stress. P = calculated average pressure. 1σ uncertainties are given in parentheses following mean values.

9. Photomicrographs of shocked pyrrhotite

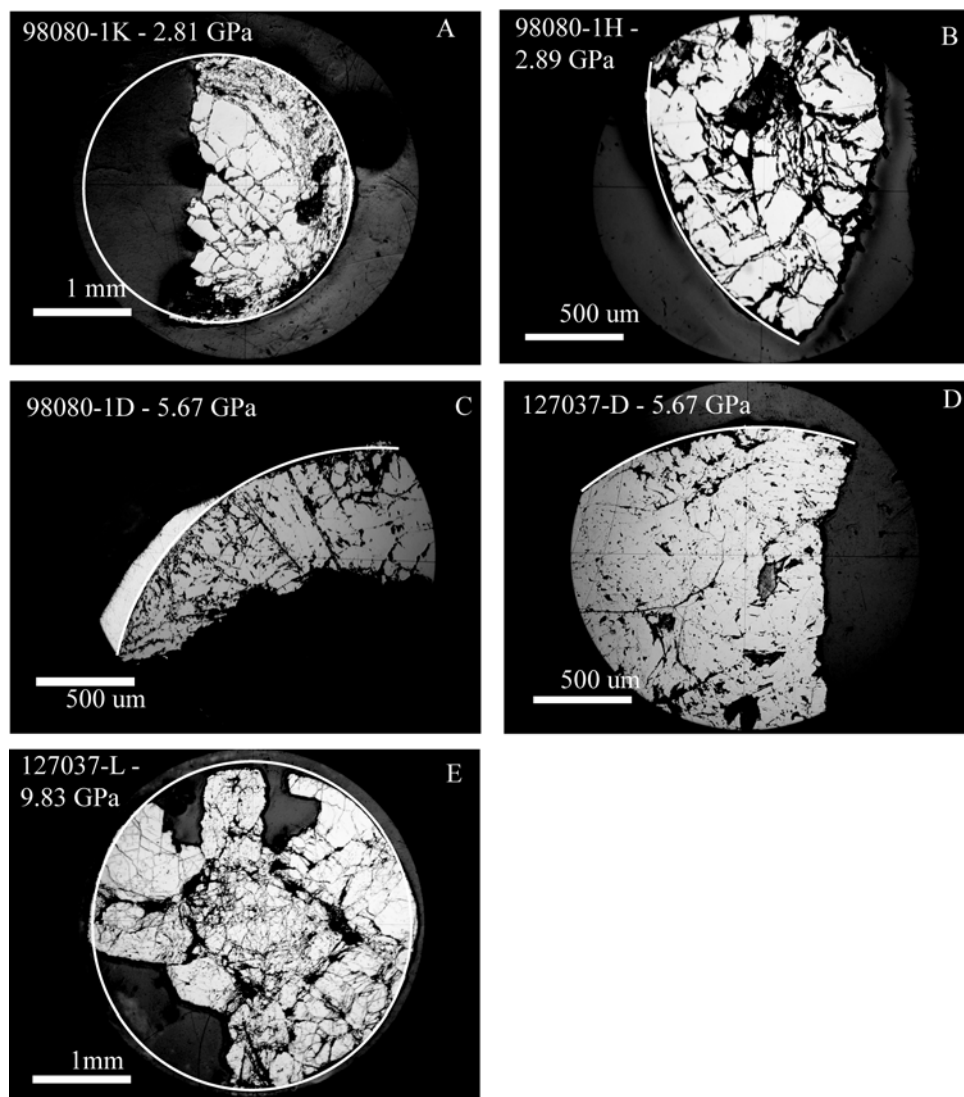


Figure S6 Photomicrographs of shocked and recovered pyrrhotite nodule (A-C) and single crystal (D and E) specimens. The white line indicates the original perimeter of the disc shaped specimen. The pressures in these samples were near enough to or above the Hugoniot Elastic Limit of pyrrhotite (~ 3 GPa) that fracturing may have occurred during compression. The nodule specimen shocked at 1.74-1.96 GPa (with uncertain pressure history) and one of the polycrystalline specimens shocked at 0.99 GPa were also broken when removed from their capsule. In these samples, tensile stresses may have exceeded the dynamic tensile strength of pyrrhotite (~ 100 s of MPa in igneous rock, Ai and Ahrens, 2004) during release due to the fact that the wave front is not a perfect step function.

10. Domain interactions

Domain interactions can be analyzed using the technique described in (1958). Deviation from idealized noninteracting single domain assemblages with uniaxial anisotropy can be described by the differential remanence, $\Delta M(H) = M_{DC}(H) - [1 - 2M_{IRM}(H)]$, where $M_{IRM}(H)$ and $M_{DC}(H)$ are the normalized magnetic moments measured during acquisition of isothermal remanent magnetization and dc backfield demagnetization of saturation isothermal remanent magnetization in a field, H , respectively. Negative ΔM values result from negative interaction yielding a net demagnetizing effect (as is the case in multidomain grains) and positive ΔM values result from positive interactions, leading to stabilization of the magnetization. If shock induced magnetic hardening is a direct result of domain-size changes, then the new domains must not interact significantly.

In the MD polycrystalline pyrrhotite (grey lines, Figure S7), the differential remanence is negative at all fields. The minimum differential remanence at low-field is less in the postshock (9.83 GPa, triangles) case than it is in the unshocked (diamonds) case. Comparisons with Figure 3 of Wehland et al. (2005) indicate that the changes are consistent with a decrease in grain size (a decrease in the net demagnetizing effect), but that the interactions in the polycrystalline pyrrhotite are of multidomain type. The changes in domain interactions in the SD/DP nodule are much more subtle, both unshocked and shocked differential remanences are very small (negative) indicating that the nodule consists of nearly entirely noninteracting single-domains consistent with its uniaxial magnetic anisotropy (linear magnetic fabric).

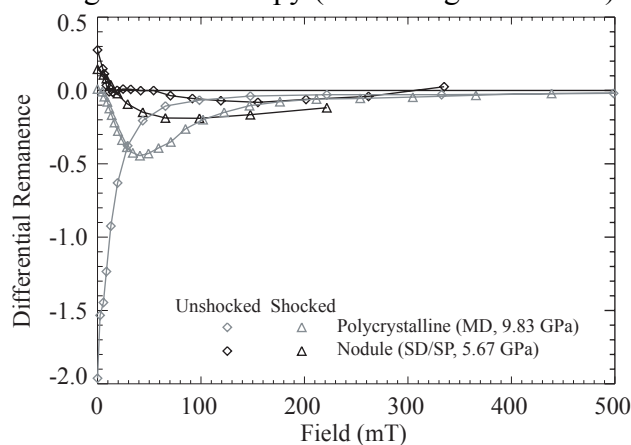


Figure S7 Differential remanence of unshocked (diamonds) and shocked (9.83 GPa) triangles MD single crystal pyrrhotite. Negative ΔM values indicate multidomain type interactions.

11. Magnetic imaging of the pyrrhotite nodule

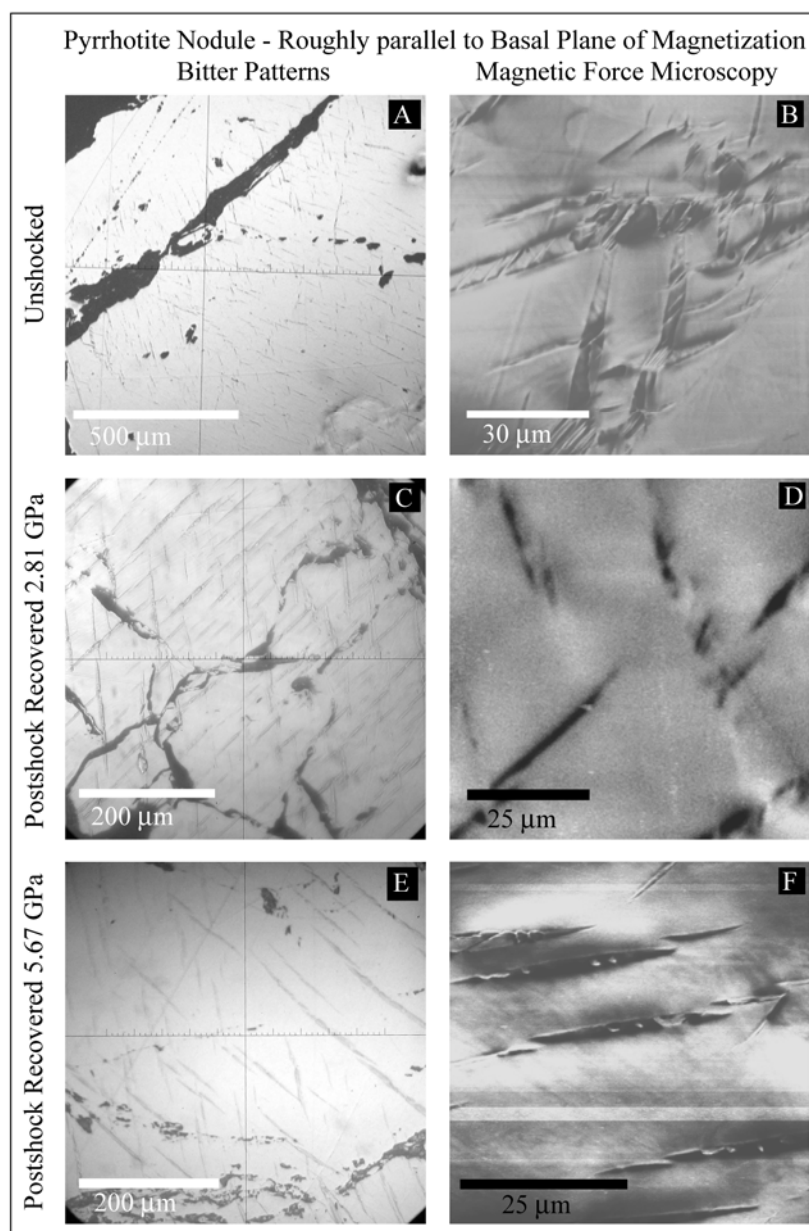


Figure S8 Magnetic imaging of polished (0.02 μm thick) (**A, B**) unshocked and (**C-F**) postshock recovered SD/SP pyrrhotite, with the shock direction roughly parallel to the basal plane for all samples. Postshock samples are AF demagnetized in 85 mT peak fields. Horizontal lines in (**F**) are an artifact of tracking error.

12. References

- Ahrens, T.J., 1979. Equations of State of Iron Sulfide and Constraints on the Sulfur Content of the Earth. *JGR* 84, 985-998.
- Ai, H.-A., Ahrens, T.J., 2004. Dynamic tensile strength of terrestrial rocks and application to impact cratering. *MAPS* 39 (2), 233-246.
- Barker, L.M., Hollenbach, R.E., 1972. Laser interferometer for measuring high velocities of any reflecting surface. *Journal of Applied Physics* 43, 4669-4675.
- Boslough, M.B., Asay, J.R., 1993. Chapter 2: Basic Principles of Shock Compression, in: Asay, J.R., M., S. (Eds), *High-Pressure Shock Compression of Solids*. Springer-Verlag, New York, pp. 7-42.
- Coe, R.S., 1966. Analysis of Magnetic Shape Anisotropy Using Second-Rank Tensors. *JGR* 71 (10), 2637-2644.
- Dekkers, M.J., 1988. Magnetic properties of natural pyrrhotite Part I: Behaviour of initial susceptibility and saturation-magnetization-related rock-magnetic parameters in a grain-size dependent framework. *PEPI* 52, 376-393.
- Gattacceca, J., Lamali, A., Rochette, P., Boustie, M., Berthe, L., 2007. The effects of explosive-driven shocks on the natural remanent magnetization and the magnetic properties of rocks. *PEPI* 162, 85-98, doi:10.1016/j.pepi.2007.1003.1006.
- Jelínek, V., 1973. Precision A.C. bridge set for measuring magnetic susceptibility of rocks and its anisotropy. *Studia Geophysica & Geodaetica* 17, 36-48, doi:10.1007/BF01614027.
- Jelínek, V., 1981. Characterization of the magnetic fabric of rocks. *Tectonophysics* 79, T63-T67, doi:10.1016/0040-1951(81)90110-4.
- Marsh, S.P., (Ed) *LASL Shock Hugoniot Data*, University of California Press, Berkeley, California, 1980, 658 pp.
- Martín-Hernández, F., Dekkers, M.J., Bominaar-Silkens, I.M.A., Maan, J.C., 2008. Magnetic anisotropy behaviour of pyrrhotite as determined by low- and high-field experiments. *GJI* 174, 42-54, doi: 10.1111/j.1365-246X.2008.03793.x.
- McGlaun, J.M., Thompson, S.L., Elrick, M.G., 1990. CTH: A 3-dimensional shock-wave physics code. *Int. J. Impact Eng.* 10, 351-360, doi:10.1016/0734-743X(90)90071-3.
- Melosh, H.J., 1989. *Impact Cratering: A Geologic Process*, Oxford University Press, New York.
- Nkoma, J.S., Ekosse, G., 1999. X-ray diffraction of chalcopyrite CuFeS_2 , pentlandite $(\text{Fe,Ni})_9\text{S}_8$ and pyrrhotite Fe_{1-x}S obtained from Cu-Ni ore bodies. *Journal of Physics: Condensed Matter* 11, 121-128.
- Louzada, K.L., et al., Shock and static pressure demagnetization of pyrrhotite and implications for the Martian crust, *Earth Planet. Sci. Lett.* (2009), doi:10.1016/j.epsl.2009.12.006

Wehland, F., Stancu, A., Rochette, P., Dekkers, M.J., Appel, E., 2005. Experimental evaluation of magnetic interaction in pyrrhotite bearing samples. *PEPI* 153, 181-190, doi:10.1016/j.pepi.2005.05.006.

Wohlfarth, E.P., 1958. Relations between different modes of the acquisition of the remanent magnetization of ferromagnetic particles. *Journal of Applied Physics* 29, 595-596.